Diagnosing the thickness-weighted averaged eddy-mean flow interaction in an eddying North Atlantic ensemble

Takaya Uchida[1*], Quentin Jamet[1], William Dewar[1,2], Dhruv Balwada[3], Julien Le Sommer[1]& Thierry Penduff[1]

[1]Institut des Géosciences de l'Environnement, Centre National de la Recherche Scientifique, France

[2]Department of Earth, Ocean and Atmospheric Science, Florida State University, USA

[3]School of Oceanography, University of Washington, USA

Key Points:

- Eddying ensemble runs of the North Atlantic Ocean are used to diagnose the thickness-weighted averaged eddy-mean flow interaction.
- The Eliassen-Palm flux divergence, which is directly related to the eddy Ertel potential vorticity (PV) flux, tends to shift the Gulf Stream northward.
- The eddy Ertel PV flux can be reconstructed with the local-gradient flux of the residual-mean Ertel PV via an anisotropic eddy diffusivity tensor.

*

Corresponding author: Takaya Uchida, `takaya.uchida@univ-grenoble-alpes.fr`

Abstract

The thickness-weighted average (TWA) framework, which treats the residual-mean flow as the prognostic variable, provides a clear theoretical understanding of the eddy feedback onto the residual-mean flow. The averaging operator involved in the TWA framework, although in theory being an ensemble mean, in practice has often been approximated by a temporal mean, which conflates the temporal variability with the eddies. Here, we analyze an ensemble of North Atlantic simulations at mesoscale permitting resolution (1/12°). We therefore recognize means and eddies in terms of ensemble means and fluctuations about those means, in keeping with the TWA formalism proposed by Young (2012). Eddy-mean flow feedbacks are encapsulated in the Eliassen-Palm (E-P) flux tensor and its divergence indicates that the eddies contribute to the zonal meandering of the Gulf Stream and its deceleration in the meridional direction. We also show that the eddy Ertel potential vorticity (PV) flux can be parametrized as an isopycnic local-gradient flux of the residual-mean Ertel PV via an anisotropic eddy diffusivity tensor. As the E-P flux divergence and eddy Ertel PV flux are directly related to one another, this provides a new pathway forward for a unified mesoscale eddy closure scheme.

Plain Language Summary

We have greatly benefited from global climate simulations in gaining insight into what the climate would look like in an ever warming future. Due to computational constraints, however, the oceanic component of such simulations have been poorly constrained; the storm systems in the ocean, often referred to as eddies, have the spatial scales of roughly several tens of kilometers and simulating the currents associated with eddies accurately on a global scale, which is on the order of thousands of kilometers, has remained challenging. Although relatively small in scale compared to the global Earth, eddies have been known to modulate the climate by transporting heat from the equator to the poles. By running a regional simulation of the North Atlantic Ocean and taking advantage of recent theoretical developments, we provide a new pathway in improving the representation of these eddies and as such, improving global ocean and climate simulations.

1 Introduction

Eddy-mean flow interaction has been a key framework in understanding jet formation in geophysical flows such as in the atmosphere and ocean (e.g. Vallis, 2017, Chapters 12 and 15). A prominent example of such a jet in the North Atlantic ocean is the

Gulf Stream. Previous studies have shown how eddies fluxing buoyancy and momentum back into the mean flow energize the Gulf Stream (Lévy et al., 2010; Waterman & Lilly, 2015; Chassignet & Xu, 2017; Aluie et al., 2018). Basin-scale simulations, however, often lack sufficient spatial resolution to accurately resolve the eddies and hence, result in underestimating the eddy fluxes of momentum and tracers (Capet et al., 2008; Arbic et al., 2013; Kjellsson & Zanna, 2017; Balwada et al., 2018; Uchida et al., 2019; Schubert et al., 2020). Due to computational constraints, we will continue to rely on models which only partially resolve the mesoscale, a scale roughly on the order of O(20-200 km) at which the ocean currents are most energetic (Stammer, 1997; Xu & Fu, 2011, 2012; Ajayi et al., 2020), for global ocean and climate simulations. As a result, there has been an ongoing effort to develop energy-backscattering eddy parametrizations which incorporate the dynamical effects of eddy momentum fluxes due to otherwise unresolved mesoscale turbulence (e.g. Kitsios et al., 2013; Zanna et al., 2017; Berloff, 2018; Bachman et al., 2018; Bachman, 2019; Jansen et al., 2019; Perezhogin, 2019; Zanna & Bolton, 2020; Juricke et al., 2020).

There has been less emphasis, however, on quantifying the spatial and temporal characteristics of the eddy buoyancy and momentum fluxes themselves, which the parametrizations are deemed to represent. The focus of this study is, therefore, to examine the dynamical effects of mesoscale turbulence on the mean flow in realistic, partially air-sea coupled, eddying ensemble runs of the North Atlantic. The thickness-weighted average (TWA) framework developed by de Szoeke and Bennett (1993), McDougall and McIntosh (2001), Young (2012), J. R. Maddison and Marshall (2013) and Aoki (2014) treats the residual-mean velocity as a prognostic variable and allows for a straightforward theoretical understanding of the eddy feedback onto the (residual) mean flow; the TWA framework has been fruitful in examining eddy-mean flow interaction in idealized modelling studies (e.g. D. P. Marshall et al., 2012; Cessi & Wolfe, 2013; Ringler et al., 2017; Bire & Wolfe, 2018). Here, we extend these studies to a realistic simulation of the North Atlantic.

To our knowledge, Aiki and Richards (2008), Aoki et al. (2016) and Zhao and Marshall (2020) are the only studies that diagnose the TWA framework in realistic ocean simulations. Aiki and Richards (2008), however, recompute the hydrostatic pressure using potential density for their off-line diagnosis in defining their buoyancy coordinate, which can result in significant discrepancies from the pressure field used in their on-line calculation and consequently errors in the diagnosed geostrophic shear. Although Aoki et al. (2016) negate this complication between the buoyancy coordinate and mean pressure field by analyzing their outputs in geopotential coordinates, they compute the eddy component of the pressure term (F^+ in their paper) using potential density, resulting in errors in the interfacial form stress (viz. this violates equation (9) described below for ϕ' and m'). The usage of geopotential coordinates also limits the eddy terms to second-order accuracy. Lastly, all three studies assume ergodicity. The ergodic assumption of treating a temporal mean equivalent to an ensemble mean, although a pragmatic one, prevents examining the temporal evolution of the residual mean fields and conflates temporal variability with the eddies, which can have leading-order consequences in quantifying the energy cycle. By adjusting the temporal mean from monthly to annual, Aiki and Richards (2008, cf. Table 2 in their paper) show that the amount of kinetic and potential energy stored in the mean and eddy reservoirs can change by up to a factor of four. Eddy-mean flow interaction in the TWA framework, hence, warrants further investigation, and we believe our study is the first to strictly implement an ensemble mean in this context.

When discussing *eddy* versus *mean flow*, one of the ambiguities lies in how the two are decomposed (Bachman et al., 2015). As noted above, often, the eddies are defined from a practical standpoint as the deviation from a temporally and/or spatially coarse-grained field regardless of the coordinate system (e.g. Aiki & Richards, 2008; Lévy et al., 2012; Sasaki et al., 2014; Griffies et al., 2015; Aoki et al., 2016; Uchida et al., 2017; Zhao & Marshall, 2020), which leaves open the question of how the filtering affects the decomposition. Due to the ensemble averaging nature of the TWA framework, we are uniquely able to define the two; the *mean flow* (ensemble mean) is the oceanic response to the surface boundary state and lateral bounday conditions, and the *eddy* (fluctuations about the ensemble mean) is the field due to intrinsic variability of mesoscale turbulence (Sérazin et al., 2017; Leroux et al., 2018).

The paper is organized as follows: We describe the model configuration in section 2 and briefly provide an overview of the TWA framework in section 3. The results are given in section 4. In particular, we highlight in section 4.2 how the Eliassen-Palm (E-P) flux divergence is related to the Ertel potential vorticity (PV) and that it can be parametrized via a local-gradient flux closure. Discussion and conclusions are given in section 5.

2 Model description

We use the model outputs from the realistic runs described in Jamet et al. (2019b) and Jamet et al. (2020), which are 24 air-sea partially coupled ensemble members of the North Atlantic ocean at mesoscale permitting resolution (1/12°) using the hydrostatic configuration of the Massachusetts Institute of Technology general circulation model (MITgcm; J. Marshall et al., 1997). We have 46 vertical levels increasing from 6 m near the surface to 250 m at depth. Harmonic, biharmonic horizontal and vertical viscosity values of $A_{\mathrm{h2}} = 20$ m^2 s^{-1}, $A_{\mathrm{h4}} = 10^{10}$ m^4 s^{-1} and $A_{\mathrm{v}} = 10^{-5}$ m^2 s^{-1} were used respectively. For completeness, we provide a brief summary of the configuration below.

Figure 1 shows the bathymetry of the modelled domain extending from 20°S to 55°N. In order to save computational time and memory allocation, the North Atlantic basin was configured to zonally wrap around periodically. Open boundary conditions are applied at the north and south boundaries of our domain and Strait of Gibraltar, such that oceanic velocities ($\mathbf{u}$) and tracers (θ, s) are restored with a 36 minutes relaxation time scale toward a state derived by an ocean-only global Nucleus for European Modelling of the Ocean (NEMO) simulation (Molines et al., 2014, ORCA12.L46-MJM88 run in their paper, hereon referred to as ORCA12). The open boundary conditions are prescribed every five days from the ORCA12 run and linearly interpolated in between. A sponge layer is further applied to two adjacent grid points from the open boundaries where model variables are restored toward boundary conditions with a one-day relaxation time scale. In total, relaxation is applied along three grid points from the boundaries with it being the strongest at the boundary. Although relatively short, no adverse effects were apparent upon inspection in response to these relaxation time scales; e.g. changes in the open boundary conditions were seen to induce a physically consistent Atlantic Meridional Overturning Circulation response inside the domain (Jamet et al., 2020).

The 24-member ensemble was constructed as follows: 24 oceanic states separated by 48 hours each were taken during an initial month-long integration beginning December 8, 1962, upon which 24 simulations were run using these as the initial conditions under a yearly *repeating* atmospheric and boundary condition of 1963. At the surface, the ocean is partially coupled to an atmospheric boundary layer model (CheapAML; Deremble et al., 2013). In CheapAML, atmospheric surface temperature and relative humidity respond to ocean surface structures by exchanges of heat and humidity computed according to the Coupled Ocean–Atmosphere Response Experiment (COARE3; Fairall et

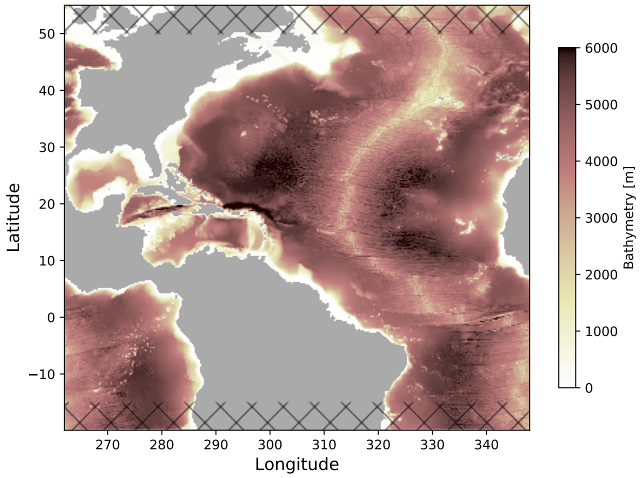

Figure 1. Bathymetry of the modelled domain. The domain was configured to wrap around zonally in order to save computation and memory allocation when generating the ensemble. The hatches indicate the northern and southern regions excluded from our analysis.

al., 2003) flux formula, but are strongly restored toward prescribed values over land; there are no zonally propagating signals of climate teleconnection. The prescribed atmospheric state is taken from the Drakkar forcing set and boundary forcing from the ORCA12 run (details are given in Jamet et al., 2019a). After a year of integration from the 24 states, the last time step from each simulation was taken as the initial condition for the 24 ensemble members; each spun-up initial oceanic state is physically consistent with the atmospheric and boundary conditions of January 1, 1963 (details are given in Jamet et al., 2020). The 24 ensemble members are then integrated forward in time for 50 years (1963-2012), and exposed to the same realistic forcing across all ensemble members. (Note that the boundary forcings are no longer cyclic after the spin-up phase.) During this interval, the oceanic state and the atmospheric boundary layer temperature and humidity evolve in time. In the following, we interpret the ensemble mean as the ocean response to the atmospheric state prescribed within the atmospheric boundary layer as well as the oceanic conditions imposed at the open boundaries of the regional domain, while the ensemble spread is attributed to intrinsic ocean dynamics that develop at mesoscale-permitting resolution (Sérazin et al., 2017; Leroux et al., 2018; Jamet et al., 2019b).

The model outputs were only saved as five-day averages. From a probabilistic perspective, the five-day averaging results in more Gaussian-like eddy statistics (based on the central-limit theorem). From a dynamical point of view, this does not allow us to close the residual-mean and eddy budgets (cf. G. Stanley, 2018, Section 4.4). Nevertheless, we believe the ensemble dimension of our dataset provides an unique opportunity to examine the TWA eddy-mean flow interaction and its implication on mesoscale closure schemes. In the context of eddy parametrizations, which we discuss in section 4.2, some temporal averaging is appropriate in order to filter out temporal scales shorter than the mesoscale eddies themselves. In the following analysis, we exclude the northern and southern extent of 5° and from our analysis and use the last five years of output (2008-2012) to avoid effects from the open boundary conditions and sponge layer (Figure 1), and to maximize the intrinsic variability amongst the ensemble members respectively.

3 Theory and implementation of thickness-weighted averaging

The ocean is a stratified fluid, and the circulation and advection of tracers tend to align themselves along the stratified density surfaces. Hence, a natural way to understand the circulation is to consider the variables in a buoyancy framework and the residual-mean flow rather than the Eulerian mean flow. We leave the detailed derivation of the TWA framework to Young (2012) and here, only provide a brief summary; the primitive equations in geopotential coordinates are first transformed to buoyancy coordinates upon which a thickness weighting and ensemble averaging along constant buoyancy surfaces are applied to obtain the TWA governing equations. Following the notation by Young (2012) and Ringler et al. (2017), the TWA horizontal momentum equations in the buoyancy coordinate system $(\tilde{t}, \tilde{x}, \tilde{y}, \tilde{b})$ are:

$$\hat{u}_{\tilde{t}} + \hat{u}\hat{u}_{\tilde{x}} + \hat{v}\hat{u}_{\tilde{y}} + \hat{\varpi}\hat{u}_{\tilde{b}} - f\hat{v} + \overline{m}_{\tilde{x}} = -\overline{\mathbf{e}}_1 \cdot (\tilde{\nabla} \cdot \mathbf{E}) + \hat{\mathcal{X}} \tag{1}$$

$$\hat{v}_{\tilde{t}} + \hat{u}\hat{v}_{\tilde{x}} + \hat{v}\hat{v}_{\tilde{y}} + \hat{\varpi}\hat{v}_{\tilde{b}} + f\hat{u} + \overline{m}_{\tilde{y}} = -\overline{\mathbf{e}}_2 \cdot (\tilde{\nabla} \cdot \mathbf{E}) + \hat{\mathcal{Y}} \tag{2}$$

where $\overline{(\cdot)}$ and $\widehat{(\cdot)} \stackrel{\text{def}}{=} \overline{\sigma}^{-1}\overline{\sigma(\cdot)}$ are the ensemble averaged and TWA variables respectively where $\sigma(= \zeta_{\tilde{b}})$ is the thickness and ζ the depth of an iso-surface of buoyancy. The subscripts denote partial derivatives. The Montgomery potential is $m = \phi - \tilde{b}\zeta$ where ϕ is the dynamically active part of hydrostatic pressure. The vectors $\overline{\mathbf{e}}_1 = \mathbf{i} + \overline{\zeta}_{\tilde{x}}\mathbf{k}$ and $\overline{\mathbf{e}}_2 = \mathbf{j}+\overline{\zeta}_{\tilde{y}}\mathbf{k}$ form the basis vectors spanning the buoyancy horizontal space where $\mathbf{i}$, $\mathbf{j}$ and $\mathbf{k}$ are the Cartesian geopotential unit vectors, and $\mathbf{E}$ is the E-P flux tensor described in detail in Section 4.1. Although each ensemble member has an individual basis $(\mathbf{e}_1, \mathbf{e}_2)$, the E-P flux divergence yields no cross terms upon averaging as the TWA operator commutes with the divergence of $\mathbf{E}$ (for mathematical details, see Section 3.4 in J. R. Maddison & Marshall, 2013); this allows for the tensor expression in equations (1) and (2). $\mathcal{X}$ and $\mathcal{Y}$ are the viscous and forcing terms.

One subtle yet important point involves the buoyancy coordinate ($\tilde{b}$) for a realistic, non-linear equation of state (EOS) for density (Jackett & Mcdougall, 1995). The analysis in Young (2012) implicitly assumes a linear EOS. With a realistic EOS the vertical coordinate can no longer "naively" be defined by potential density for example, and is the subject of some debate (e.g. Montgomery, 1937; Jackett & McDougall, 1997; McDougall & Jackett, 2005; de Szoeke & Springer, 2009; Klocker et al., 2009; Tailleux, 2016; Lang et al., 2020). We argue for the use of in-situ density *anomaly* ($\delta \overset{\text{def}}{=} \rho - \underset{\sim}{\rho}(\zeta)$ where ρ is the in-situ density and $\underset{\sim}{\rho}$ is a function of only depth; Montgomery, 1937) for practical reasons provided below in order to remove the effect of compressibility; other choices can be made (G. J. Stanley, 2019b, 2019a). The formulation of in-situ density anomaly is analogous to where $\underset{\sim}{\rho} \rightarrow \frac{d}{dz}\int \rho_0 dz$ and the anomaly reduces to $\delta = \rho - \rho_0$ for a linear EOS where $\rho_0 = 999.8$ kg m^{-3} is the Boussinesq reference density prescribed in MITgcm. The buoyancy can then be defined as:

$$\underset{\sim}{b} = -\frac{g}{\rho_0}\delta \overset{\text{def}}{=} \tilde{b} \tag{3}$$

where $\tilde{b}$ denotes the vertical coordinate. The question becomes how to choose $\underset{\sim}{\rho}(\zeta)$ so that monotonicity is maintained ($\tilde{b}_\zeta > 0$). The vertical derivative of the in-situ density anomaly can be decomposed as:

$$\delta_\zeta = \rho_\zeta - \frac{d}{d\zeta}\underset{\sim}{\rho} = \rho_\Phi \frac{d\Phi}{d\zeta} - \frac{d}{d\zeta}\underset{\sim}{\rho} = \frac{-\rho_0 g}{c_s^2} - \frac{d}{d\zeta}\underset{\sim}{\rho}, \tag{4}$$

where $\Phi = -g\zeta$ is the dynamically non-active part of hydrostatic pressure and c_s is the sound speed. For simplicity, we can write $\frac{d}{d\zeta}\underset{\sim}{\rho} \overset{\text{def}}{=} -\rho_0 g \mathcal{C}_s^{-2}$ where $\mathcal{C}_s = \mathcal{C}_s(\zeta)$ is a function of only depth, which yields:

$$\tilde{b}_\zeta = -\frac{g}{\rho_0}\delta_\zeta = g^2 \frac{\mathcal{C}_s^2 - c_s^2}{c_s^2 \mathcal{C}_s^2}. \tag{5}$$

Denoting $\mathcal{C}_s = c_s + \Delta$ where $c_s^{-1}\Delta \ll 1$, the right-hand side (RHS) of equation (5) becomes:

$$g^2 \frac{(c_s + \Delta)^2 - c_s^2}{c_s^2 \mathcal{C}_s^2} \approx \frac{g^2}{\mathcal{C}_s^2}\Big[\big(1 + \frac{2\Delta}{c_s}\big) - 1\Big] = \frac{2g^2\Delta}{c_s \mathcal{C}_s^2} \sim O(10^{-6}). \tag{6}$$

Hence, so long as $\mathcal{C}_s \gtrsim c_s$, monotonicity is assured while removing a large portion of compressibility, i.e. the iso-surfaces of $\tilde{b}$ become close to neutral surfaces. In practice, we chose $\mathcal{C}_s$ to take the value of maximum sound speed at each depth over the entire ensemble. The buoyancy equation using the in-situ density anomaly becomes:

$$\frac{D\tilde{b}}{Dt} = \tilde{b}_\theta \dot{\theta} + \tilde{b}_s \dot{s} + \tilde{b}_\zeta \frac{D\zeta}{Dt} \tag{7}$$

$$= \mathcal{B} + wg^2 \frac{\mathcal{C}_s^2 - c_s^2}{c_s^2 \mathcal{C}_s^2}, \tag{8}$$

where $\mathcal{B} \overset{\text{def}}{=} \tilde{b}_\theta \dot{\theta} + \tilde{b}_s \dot{s}$, and $\dot{\theta}$ and $\dot{s}$ are the net diabatic contributions on potential temperature and practical salinity respectively, which we approximate by diagnosing off-line the sum of harmonic and bihamonic diffusion below the mixed layer using the five-day averaged outputs of θ and s. The RHS of (8) can be summarized as the dia-surface velocity $\varpi \overset{\text{def}}{=} \mathcal{B} + wg^2 \frac{\mathcal{C}_s^2 - c_s^2}{c_s^2 \mathcal{C}_s^2}$. A further requirement of the TWA framework is that the pressure anomaly defined by such buoyancy coordinate transforms into a body force in the buoyancy coordinate:

$$\nabla_\mathrm{h} \underset{\sim}{\phi}(\tilde{b}) = \tilde{\nabla}_\mathrm{h} m. \tag{9}$$

Using the in-situ buoyancy anomaly, the pressure anomaly becomes:

$$\underset{\sim}{\phi} = \int \tilde{b}\; d\zeta, \tag{10}$$

while the pressure anomaly for a Boussinesq hydrostatic fluid is:

$$\phi = \int -\frac{g}{\rho_0}(\rho - \rho_0)\; d\zeta. \tag{11}$$

Since $\underset{\sim}{\rho}$ is only a function of depth, the horizontal gradient of the two remain identical ($\nabla_\mathrm{h} \underset{\sim}{\phi} = \nabla_\mathrm{h} \phi$) and equation (9) holds. (We note that equation (9) does not hold for pressure anomaly defined by potential density when the EOS is non-linear, and is non-trivial for other density variables such as neutral and orthobaric densities.) The use of in-situ density anomaly to define the buoyancy coordinate maintains the desirable properties of a unique, statically stable vertical coordinate and a simple hydrostatic balance ($\sigma = \zeta_{\tilde{b}} = -m_{\tilde{b}\tilde{b}}$) while removing more than 99% of the effect of compressibility basin wide at each depth as $\mathcal{C}_s$ is global variable ($\frac{g^2(c_s^{-2} - \mathcal{C}_s^{-2})}{g^2 c_s^{-2}} \approx \frac{2c_s\Delta}{\mathcal{C}_s^2} \sim O(10^{-2})$). For a non-linear EOS, a material conservation of potential vorticity (PV) and non-acceleration conditions do not exist (cf. Vallis, 2017, Chapter 4). Discussion regarding the energetics are given in Appendix A.

The raw simulation outputs were in geopotential coordinates so we first remapped all of the variables in equations (1) and (2) onto 60 buoyancy levels spread across the range of $\tilde{b} \in (-0.2826, -0.2060)$ m s^{-2} (with the mathematical formulation of $\delta = \delta_0 + A_\delta \frac{\tanh{(\tau)}}{\tanh{(\tau_\mathrm{max})}}$ where $\delta_0 = 21$ kg m^{-3}, $A_\delta = 7.8$ kg m^{-3}, and $\tau \in [0, 2)$ in order to account for the abyssal weak stratification):

$$(\mathbf{u}, \underset{\sim}{b}, \nabla_{\mathrm{h}}\underset{\sim}{\phi}, \theta, s, \varpi)(t, x, y, z) \longmapsto (\mathbf{u}, \zeta, \tilde{\nabla}_{\mathrm{h}} m, \theta, s, \varpi)(\tilde{t}, \tilde{x}, \tilde{y}, \tilde{b}) \tag{12}$$

using the `fastjmd95` Python package to compute the in-situ density and its partial derivatives (Abernathey, 2020), and the `xlayers` Python package (Jones, 2019; Jones et al., 2020) which implements the MITgcm layers package off-line and allows for coordinate remapping consistent with the finite-volume discretization. The horizontal velocity vector is $\mathbf{u} = u\mathbf{i} + v\mathbf{j} = u\mathbf{e}_1 + v\mathbf{e}_2$. For the horizontal pressure anomaly gradient, we have invoked the identity:

$$\nabla_{\mathrm{h}}\underset{\sim}{\phi}(z) \longmapsto \nabla_{\mathrm{h}}\underset{\sim}{\phi}(\tilde{b}) = \tilde{\nabla}_{\mathrm{h}} m \tag{13}$$

where the subscript $(\cdot)_{\mathrm{h}}$ represents the horizontal gradient and $\tilde{\nabla}_{\mathrm{h}} = (\partial_{\tilde{x}}, \partial_{\tilde{y}})$ and we re-computed the pressure anomaly using the five-day averaged outputs.

4 Results

We start by showing the time series of domain-averaged horizontal kinetic energy (KE) and potential temperature (Figure 2a). Figure 2a shows the simulation has a prominent seasonal cycle with a slight cooling trend. In Figure 2, we also show the (residual) mean fields on January 3, 2008, the first day of the five years of output we analyze. The depth of the buoyancy level shown in Figure 2c is below the ensemble-mean mixed-layer depth (MLD; Figure 2b) basin wide where diabatic effects are small. We focus on this buoyancy level for the remainder of this study as it is below the MLD and the iso-surface of buoyancy does not outcrop but is shallow enough to capture the imprint of the Gulf Stream and eddies; the iso-surface shoals drastically across the latitude of 38°N where the separated Gulf Stream is situated (Figure 2d). The ensemble-mean MLD was computed as the depth at which the potential density computed from ensemble-mean temperature and salinity fields increased by 0.03 kg m^{-3} from the density at 10 m depth ($\overline{\mathrm{MLD}} \stackrel{\mathrm{def}}{=} \mathrm{MLD}(\overline{\theta}, \overline{s})$; de Boyer Montégut et al., 2004). The mean KE field ($K^{\#} \stackrel{\mathrm{def}}{=} |\hat{\mathbf{u}}|^2/2$; Figure 2d) shows the characteristic features of the Gulf Stream, North Brazil Current and equatorial undercurrent. The mean Rossby number ($\mathrm{Ro}^{\#} \stackrel{\mathrm{def}}{=} f^{-1}(\hat{v}_{\tilde{x}} - \hat{u}_{\tilde{y}})$) shown in Figure 2e is smaller than unity except for near the equator where the Coriolis parameter becomes small, indicating that over most of the North Atlantic basin, the mean flow in the interior is balanced. The kinematics of discretizing the gradients in buoyancy coordinates are given in Appendix B. We now move on to examine the eddy feedback onto the mean flow.

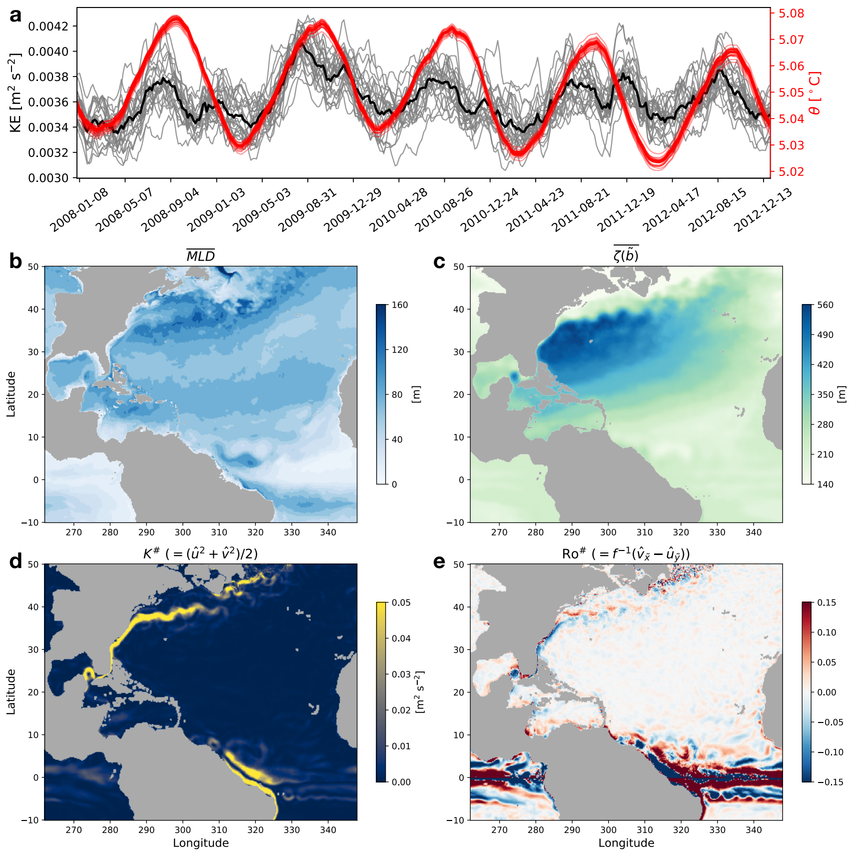

Figure 2. Time series of the domain-averaged KE (black) and potential temperature (red) for the 24 ensemble members between 10°S-50°N. The thick lines show the ensemble mean and the thin lines each ensemble member **a**. **b**,**c** The ensemble-mean MLD on January 3, 2008 and depth of the iso-surface of buoyancy $\tilde{b} = -0.260$ m s^{-2}. **d**,**e** The residual-mean kinetic energy ($K^\#$) and Rossby number (Ro$^\#$) on the same buoyancy surface.

4.1 The Eliassen-Palm flux tensor

The E-P flux tensor ($\mathbf{E}$) in the TWA framework (eqns. (1) and (2)) is:

$$\mathbf{E} = \begin{pmatrix} \widehat{u''u''} + \frac{1}{2\overline{\sigma}}\overline{\zeta'^2} & \widehat{u''v''} & 0 \\ \widehat{v''u''} & \widehat{v''v''} + \frac{1}{2\overline{\sigma}}\overline{\zeta'^2} & 0 \\ \widehat{\varpi''u''} + \frac{1}{\overline{\sigma}}\overline{\zeta' m'_{\tilde{x}}} & \widehat{\varpi''v''} + \frac{1}{\overline{\sigma}}\overline{\zeta' m'_{\tilde{y}}} & 0 \end{pmatrix} \tag{14}$$

where $(\cdot)'' = (\cdot) - \widehat{(\cdot)}$ and $(\cdot)' = (\cdot) - \overline{(\cdot)}$ are the residual of instantaneous snapshot outputs from the thickness-weighted and ensemble averages respectively (J. R. Maddison & Marshall, 2013; Aoki, 2014; Ringler et al., 2017). The two are related via the (eddy-induced) quasi-Stokes velocity (Greatbatch, 1998; McDougall & McIntosh, 2001):

$$\mathbf{u}'' = \mathbf{u} - \frac{\overline{\sigma\mathbf{u}}}{\overline{\sigma}} = \overline{\mathbf{u}} + \mathbf{u}' - \frac{\overline{(\overline{\sigma} + \sigma')(\overline{\mathbf{u}} + \mathbf{u}')}}{\overline{\sigma}} \tag{15}$$

$$= \mathbf{u}' + \frac{\overline{\sigma'\mathbf{u}'}}{\overline{\sigma}}. \tag{16}$$

We show each term in equation (14) in Figure 3. The Reynolds stress term $\widehat{u''v''}$ is associated with barotropic processes (Figure 3a; Vallis, 2017, Chapter 15). The eddy momentum flux terms $\widehat{|\mathbf{u}''|^2}$ in Figure 3c,d are seen to exchange momentum between eddies and the mean flow, i.e. to accelerate or decelerate the Gulf Stream. The interfacial form stress ($\overline{\zeta'\tilde{\nabla}_\mathrm{h} m'}$; Figure 3e,f) associated with baroclinic instability is "deceivingly" orders of magnitude smaller than the other terms. It is important to keep in mind, however, that it is the divergence of the E-P flux and not the flux itself that goes into the momentum equations, and the horizontal ($\tilde{\nabla}_\mathrm{h}$) and vertical gradient ($\partial_{\tilde{b}}$) differ by roughly O(10^6). The contribution from the adiabatic and compressibility effects (i.e. the terms with ϖ) were smaller than the interfacial form stress by another order of magnitude or more in the subtropics (not shown).

Writing out the E-P flux divergence in eqns. (1) and (2) gives:

$$-\overline{\mathbf{e}}_1 \cdot (\tilde{\nabla} \cdot \mathbf{E}) = -\overline{\sigma}^{-1}\Big(\big[\overline{\sigma}(\widehat{u''u''} + \frac{1}{2\overline{\sigma}}\overline{\zeta'^2})\big]_{\tilde{x}} + \big[\overline{\sigma}\widehat{v''u''}\big]_{\tilde{y}} + \big[\overline{\sigma}(\widehat{\varpi''u''} + \frac{1}{\overline{\sigma}}\overline{\zeta' m'_{\tilde{x}}})\big]_{\tilde{b}}\Big) \tag{17}$$

$$= -\overline{\sigma}^{-1}\Big([\overline{\sigma u''u''} + \overline{\zeta'^2}/2]_{\tilde{x}} + [\overline{\sigma v''u''}]_{\tilde{y}} + [\overline{\sigma\varpi''u''} + \overline{\zeta' m'_{\tilde{x}}}]_{\tilde{b}}\Big), \tag{18}$$

$$\stackrel{\text{def}}{=} -(E^{00}_{\tilde{x}} + E^{10}_{\tilde{y}} + E^{20}_{\tilde{b}}) \tag{19}$$

$$-\overline{\mathbf{e}}_2 \cdot (\tilde{\nabla} \cdot \mathbf{E}) = -\overline{\sigma}^{-1}\Big(\big[\overline{\sigma}\widehat{u''v''}\big]_{\tilde{x}} + \big[\overline{\sigma}(\widehat{v''v''} + \frac{1}{2\overline{\sigma}}\overline{\zeta'^2})\big]_{\tilde{y}} + \big[\overline{\sigma}(\widehat{\varpi''v''} + \frac{1}{\overline{\sigma}}\overline{\zeta' m'_{\tilde{y}}})\big]_{\tilde{b}}\Big) \tag{20}$$

$$= -\overline{\sigma}^{-1}\Big([\overline{\sigma u''v''}]_{\tilde{x}} + [\overline{\sigma v''v''} + \overline{\zeta'^2}/2]_{\tilde{y}} + [\overline{\sigma\varpi''v''} + \overline{\zeta' m'_{\tilde{y}}}]_{\tilde{b}}\Big), \tag{21}$$

$$\stackrel{\text{def}}{=} -(E^{01}_{\tilde{x}} + E^{11}_{\tilde{y}} + E^{21}_{\tilde{b}}). \tag{22}$$

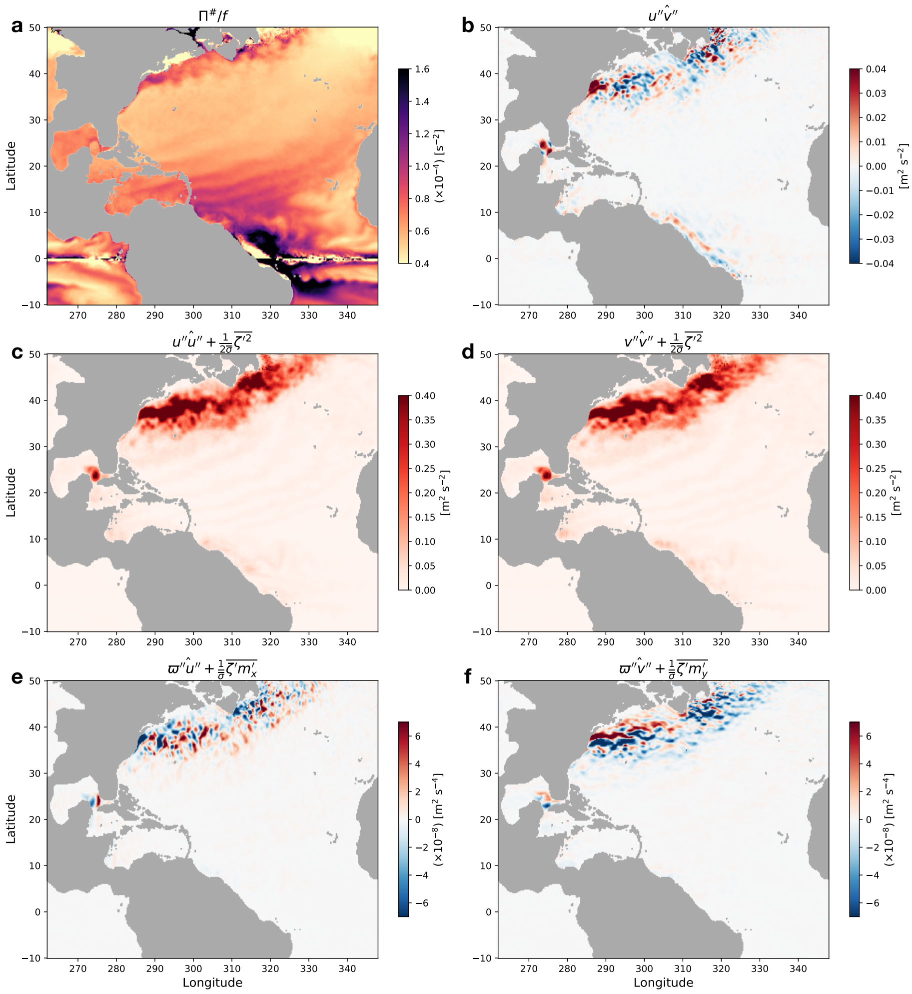

Figure 3. The residual-mean Ertel potential vorticity normalized by the local Coriolis parameter ($\Pi^{\#}/f \overset{\text{def}}{=} \overline{\sigma}^{-1}(1 + \text{Ro}^{\#})$) **a** and terms in the E-P flux tensor **b**-**f** on January 3, 2008 on the iso-surface of buoyancy as in Figure 2. Note the scaling factors on panels a, e and f.

Figure 4 shows each term in the E-P flux divergence. The first thing to note is that the signal in the separated Gulf Stream dominates over the entire North Atlantic gyre; this is consistent with Jamet et al. (2021) where they found the subtropical gyre to be a Fofonoff-like inertial circulation (Fofonoff, 1981), and that the separated jet was where the energy input from surface winds were predominantly lost to eddies. The divergence of interfacial form stress becomes larger than the divergence of the Reynolds stress term attributable to barotropic instability, which is the smallest amongst the three terms in the E-P flux divergence (Figure 4b,c) including the North Brazil Current region. It is quite surprising that the signals in the equatorial undercurrent region, although having relatively high KE (Figure 2d), are significantly smaller than in the Gulf Stream and North Brazil Current regions, virtually not visible in Figures 3 and 4. This implies that the residual-mean flow dominates over the eddies in the equatorial region.

We now examine further details in the separated Gulf Stream region. The dipole features for the zonal direction in the divergence of eddy momentum fluxes and interfacial form stress likely contribute to the jet meandering (Figure 4a,e). In the meridional direction, the eddy momentum flux divergence tends to shift the separated Gulf Stream northwards (flux momentum into the jet on the northern flank and out of it on the southern flank; Figure 4d), while the divergence of interfacial form stress (i.e. baroclinic instability) counteracts to shift the jet southwards (Figure 4f). The two tend to cancel each other out (Figure 4a,d,e,f), however, with the residual generally having the same structures as the eddy momentum flux divergence in the zonal direction (Figure 4a,g), and meridional direction (Figure 4d,h). This implies that in our model, barotropic processes dominate over baroclinic in the separated Gulf Stream, which is consistent with Jamet et al. (2021). In order to estimate the integrated net effect between the divergence of eddy momentum fluxes and interfacial form stress, we compute the volume average of them ($E_{\tilde{x}}^{00}, E_{\tilde{b}}^{20}$ and $E_{\tilde{y}}^{11}, E_{\tilde{b}}^{21}$) over buoyancy levels roughly corresponding to the depths of 300-1000 m for the northern flank (38°N-40°N; Figure 5c,d) and southern flank (36°N-38°N; Figure 5e,f) respectively over the zonal extent of 29°E-305°E where the separated Gulf Steam is roughly zonal. The separated Gulf Stream can be identified with the steep shoaling of the iso-surfaces of buoyancy between 36°N-40°N (Figure 5a,b). The overall magnitude and reversal in sign around 40°N with diminishing amplitude with depth for the zonal E-P flux divergence ($-\overline{\mathbf{e}}_1 \cdot (\tilde{\nabla} \cdot \mathbf{E})$; Figure 5a) is roughly in agreement with Ringler et al. (2017, their Figure 6 where the sign convention in equation (17) is reversed from

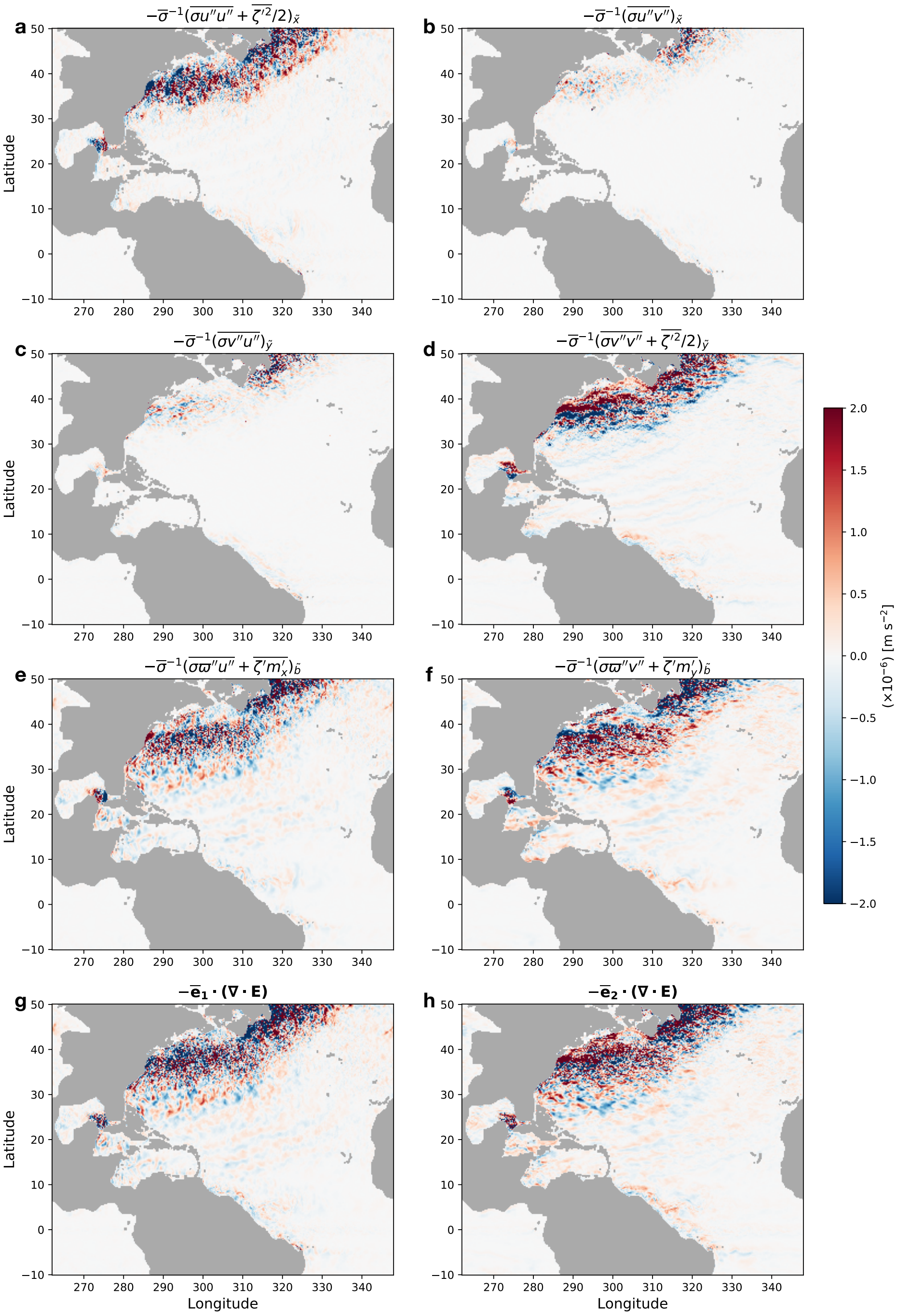

Figure 4. The terms in the divergence of E-P flux tensor on January 3, 2008 on the iso-surface of buoyancy as in Figure 2. Positive values (red shadings) indicate the eddies fluxing momentum to the mean flow and visa versa **a-f**. The panels are laid out so that summing up the top three rows per column yields the total zonal $(-\bar{\mathbf{e}}_1 \cdot (\tilde{\nabla} \cdot \mathbf{E}))$ **g** and meridional E-P flux divergence $(-\bar{\mathbf{e}}_2 \cdot (\tilde{\nabla} \cdot \mathbf{E}))$ **h** respectively.

ours for the eddy forcing term and their units are in [m s^{-1} day^{-1}]) where they diagnosed an idealized zonally re-entrant jet. We would like to note that unlike Ringler et al. (2017), we do not take the zonal mean to define the mean flow so we are able to discuss zonal inhomogeneities in the TWA structure. Figure 5c-f shows that the two tend to counteract each other with opposite signs on the northern and southern flank of the jet throughout the five years of output we analyze. The divergence of E-P flux closely follows that of eddy momentum fluxes. This counteracting balance is consistent with what Aoki et al. (2016, the terms $\partial_x R^x$ and $\partial_z(R^z + F_a^+)$ in their Figures 5a and 6) found in the Kuroshio extension region.

4.2 The Ertel potential vorticity flux

As was noted by Young (2012), the E-P flux divergence is directly related to the eddy Ertel PV flux and can be written as:

$$\overline{\mathbf{e}}_1 \cdot (\tilde{\nabla} \cdot \mathbf{E}) = -\overline{\sigma}\mathbf{F}^{\#} \cdot \mathbf{j} \ , \quad \overline{\mathbf{e}}_2 \cdot (\tilde{\nabla} \cdot \mathbf{E}) = \overline{\sigma}\mathbf{F}^{\#} \cdot \mathbf{i} \ , \tag{23}$$

where $\mathbf{F}^{\#} \stackrel{\text{def}}{=} F^{\#1}\overline{\mathbf{e}}_1 + F^{\#2}\overline{\mathbf{e}}_2 = \overline{\sigma}^{-1}\big[\{\overline{\mathbf{e}}_2 \cdot (\tilde{\nabla} \cdot \mathbf{E})\}\overline{\mathbf{e}}_1 - \{\overline{\mathbf{e}}_1 \cdot (\tilde{\nabla} \cdot \mathbf{E})\}\overline{\mathbf{e}}_2\big]$ and $\Pi^{\#} \stackrel{\text{def}}{=} \overline{\sigma}^{-1}(f + \hat{v}_{\tilde{x}} - \hat{u}_{\tilde{y}})$ are the eddy Ertel PV flux and residual-mean Ertel PV respectively. Note $\Pi^{\#}$, computed from the residual-mean velocities, is different from the TWA Ertel PV, viz. $\widehat{\Pi} = \overline{\sigma}^{-1}\overline{\sigma\Pi} = \overline{\sigma}^{-1}(f + \overline{v}_{\tilde{x}} - \overline{u}_{\tilde{y}})$ and consequently $\mathbf{F}^{\#} \neq \widehat{\mathbf{u}''\Pi''}$; the difference has to due with the cross-product operator not commuting with the TWA operator (J. R. Madison & Marshall, 2013). Equation (23) implies that if we are able to parametrize the eddy Ertel PV flux, equivalently we have parametrized the eddy feedback onto the mean flow encapsulated in the E-P flux divergence.

It is well known that i) the governing equation for Ertel PV is similar to that of passive tracers (e.g. Haynes & McIntyre, 1987, and references therein), and ii) mesoscale eddies stir passive tracers along neutral surfaces (Redi, 1982; Gnanadesikan et al., 2015; Naveira Garabato et al., 2017; Griffies, 2004; Jones & Abernathey, 2019; Uchida et al., 2020). Minimizing the effect of compressibility in the buoyancy coordinate (equation (3)) also minimizes the solenoidal baroclinicity term (viz. $\tilde{\nabla}\tilde{b} \cdot (\tilde{\nabla}\rho \times \tilde{\nabla}\phi)$; Vallis, 2017, see Section 4.5 for more details) and further primes us to treat Ertel PV as a tracer. One significant difference between Ertel PV and passive tracers, however, is in its dynamical significance; the Ertel PV feeds back onto the dynamics in the form of eddy fluxes perhaps most well known in the transformed-Eulerian mean framework (e.g. Vallis, 2017, Chapter 10). This has led to the idea that the dynamical effect of mesoscale turbulence

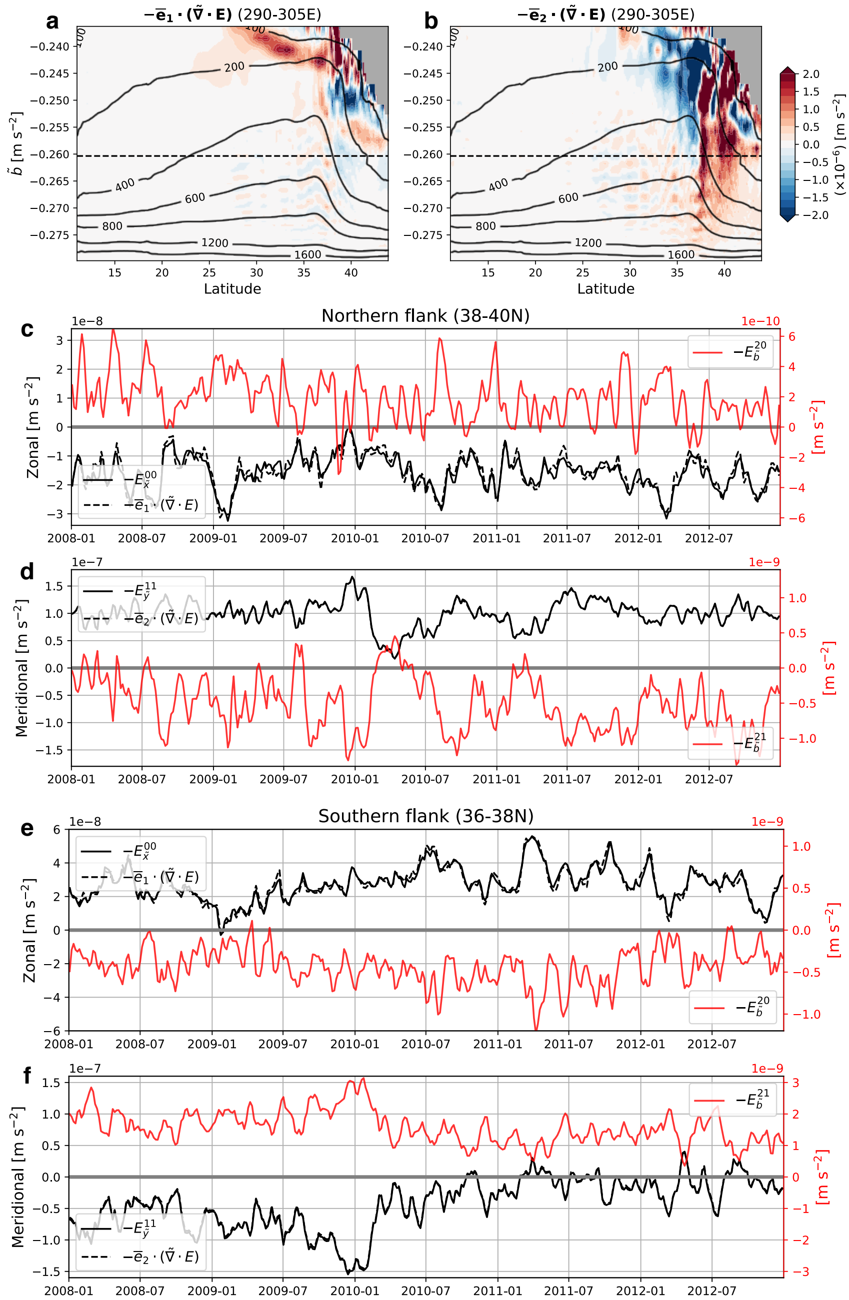

Figure 5. The zonal-mean transect between 290°E-305°E of the E-P flux divergence on January 3, 2008 is shown in colored shading and ensemble-mean depth in black contours **a**,**b**. The iso-surface of buoyancy used through Figures 2-4 is shown as the black dashed line. The masked out region north of 40N near the surface is where the iso-surfaces of buoyancy outcrop across all ensemble members. **c**-**f** Time series the volume-averaged divergence of eddy momentum flux ($-E^{00}_{\tilde{x}}$, $-E^{11}_{\tilde{y}}$; black solid), interfacial form stress ($-E^{20}_{\tilde{b}}$, $-E^{21}_{\tilde{b}}$; red solid), and E-P flux ($-\bar{\mathbf{e}}_1 \cdot (\tilde{\nabla} \cdot \mathbf{E})$, $-\bar{\mathbf{e}}_2 \cdot (\tilde{\nabla} \cdot \mathbf{E})$; black dashed). Note the order of magnitude difference between the black and red y axis.

may be parametrized as a local gradient flux of the mean Ertel PV (e.g. Killworth, 1997; Greatbatch, 1998; D. P. Marshall et al., 1999, 2012; Eden, 2010), i.e.

$$\mathbf{F}^{\#} = -\kappa \tilde{\nabla}_{\mathrm{h}} \Pi^{\#}, \tag{24}$$

where κ is the eddy diffusivity. Equations (1), (2), (23) and (24) provide a pathway for a unique solution for the eddy closure problem as the divergence of fluxes is gauge invariant (J. R. Maddison & Marshall, 2013).

While it is tempting to directly infer a scalar eddy diffusivity from equation (24), assuming an isotropic diffusivity for an anisotropic flow as in our realistic simulation is a poor approximation (R. D. Smith & Gent, 2004; Ferrari & Nikurashin, 2010; Fox-Kemper et al., 2013). We, therefore, take the approach of estimating the eddy diffusivity tensor ($\mathbf{K}$) from a least-squares best fit to (Plumb & Mahlman, 1987; Abernathey et al., 2013; Bachman & Fox-Kemper, 2013):

$$\underbrace{\begin{pmatrix} \widehat{u''\theta''} & \widehat{v''\theta''} \\ \widehat{u''s''} & \widehat{v''s''} \\ F^{\#1} & F^{\#2} \end{pmatrix}}_{\mathbf{F}} = - \underbrace{\begin{pmatrix} \hat{\theta}_{\tilde{x}} & \hat{\theta}_{\tilde{y}} \\ \hat{s}_{\tilde{x}} & \hat{s}_{\tilde{y}} \\ \Pi^{\#}_{\tilde{x}} & \Pi^{\#}_{\tilde{y}} \end{pmatrix}}_{\mathbf{G}} \cdot \underbrace{\begin{pmatrix} \kappa^{uu} & \kappa^{vu} \\ \kappa^{uv} & \kappa^{vv} \end{pmatrix}}_{\mathbf{K}} . \tag{25}$$

In studies trying to parametrize the eddy-induced fluxes of isopycnal thickness, they have the freedom to parametrize the total flux or only its divergent component as it is the eddy flux divergence that enters the buoyancy equation (e.g. Eden et al., 2007; Grooms & Kleiber, 2019). This has caused some ambiguity on how the rotational component of the eddy flux, often referred to as the gauge freedom, should be treated (discussed in depth by Griffies, 2004). However, since the TWA equations are forced directly by the eddy Ertel PV flux itself and not its divergence, we do not need to consider the discussion centred around rotational fluxes. In other words, equation (23) makes the case for parametrizing the *total* eddy flux, as opposed to solely its divergent component, when formulating a closure scheme for Ertel PV. The assumption that goes into equation (25) is that the eddy flux of temperature, salinity and Ertel PV behave statistically in a similar manner (Bachman et al., 2015). Since they are all active tracers, we would expect this assumption to hold to a good degree.

The least-squares fit can be estimated as $\mathbf{K} = \mathbf{G}^{+}\mathbf{F}$ where $\mathbf{G}^{+}$ is the Moore-Penrose psuedo inverse of $\mathbf{G}$ for each data point (Bachman et al., 2015). Although it is possible to invert equation (25) with just two tracers, the inversion becomes ill defined unless their distributions are orthogonal to one another (Bachman et al., 2015). We have, thus, kept it over-determined using three tracers. The gradients of the mean field tended to be noisy due to errors accumulating from the remapping process (equation (12)). Therefore, we applied a convolutional spatial smoothing to the mean fields $(\hat{\theta}, \hat{s}, \Pi^{\#})$ prior to taking their gradient and eddy terms (viz. each element in $\mathbf{F}$) with a 15×15 Hann filter in the horizontal grid points using the `xscale` Python package (Sérazin, 2019). The spatial smoothing can be considered similar to a numerical convergence of the fields with an increase in the number of ensemble members. Each row in $\mathbf{F}$ and $\mathbf{G}$ was then normalized by horizontal median of the magnitude of each eddy fluxes (i.e. $\frac{(\mathbf{G}^C, \mathbf{F}^C)}{\text{median}[|\mathbf{G}^C|]}$ where $\mathbf{F}^C$ is the smoothed eddy flux of an arbitrary tracer C) prior to the inversion so that each tracer had roughly equal weighting in inverting equation (25).

From Figure 4, it is evident that the equatorial region contributes little to the Gulf Stream, so we will focus on north of 20°N in this section. Figure 6a,b shows the diagnosed smoothed eddy Ertel PV flux ($\mathbf{F}^{\Pi}$), which we refer to as the "true" flux, and its reconstructed equivalent via equation (25) as a local-gradient flux of the mean Ertel PV ($\mathbf{F}^{\Pi}_{\text{reconstructed}} = \mathbf{G}^{\Pi} \cdot \mathbf{K}^{\Pi}$; Figure 6c,d). (We show the reconstruction of the eddy temperature and salinity fluxes in Figures C1 and C2.) We see that the local-gradient flux closure successfully captures the spatial features of the true flux with the residual between the two being small (Figure 6e,f). The residual comes from the smoothing we have applied prior to inverting equation (25) and/or errors in the remapping and discretization, but it is likely that this residual would decrease with an increase in the number of ensemble members. One may argue that since we are fitting the eddy diffusivities, the agreement is to be expected. It is nevertheless encouraging to see how well the eddy Ertel PV fluxes can be represented via an anisotropic eddy diffusivity tensor (Figure 7) compared to previous studies reconstructing the eddy tracer fluxes with a scalar diffusivity (e.g. Wilson & Williams, 2006; Eden & Greatbatch, 2008; J. Maddison et al., 2015; Mak et al., 2016). This also provides confidence to the assumption behind equation (25) that Ertel PV behaves similarly to active tracers along buoyancy contours. In other words, along with the TWA framework, we have chosen the appropriate regression model to relate the total eddy transport of active tracers to their mean fields.

The diffusivities presented in Figure 7a-d are roughly on the same order as previous estimates based on satellite products (J. Marshall et al., 2006; Abernathey & Marshall, 2013; Klocker & Abernathey, 2014; Busecke et al., 2017; Bolton et al., 2019), in-situ observations (Cole et al., 2015; Roach et al., 2018; Groeskamp et al., 2020), and mod-

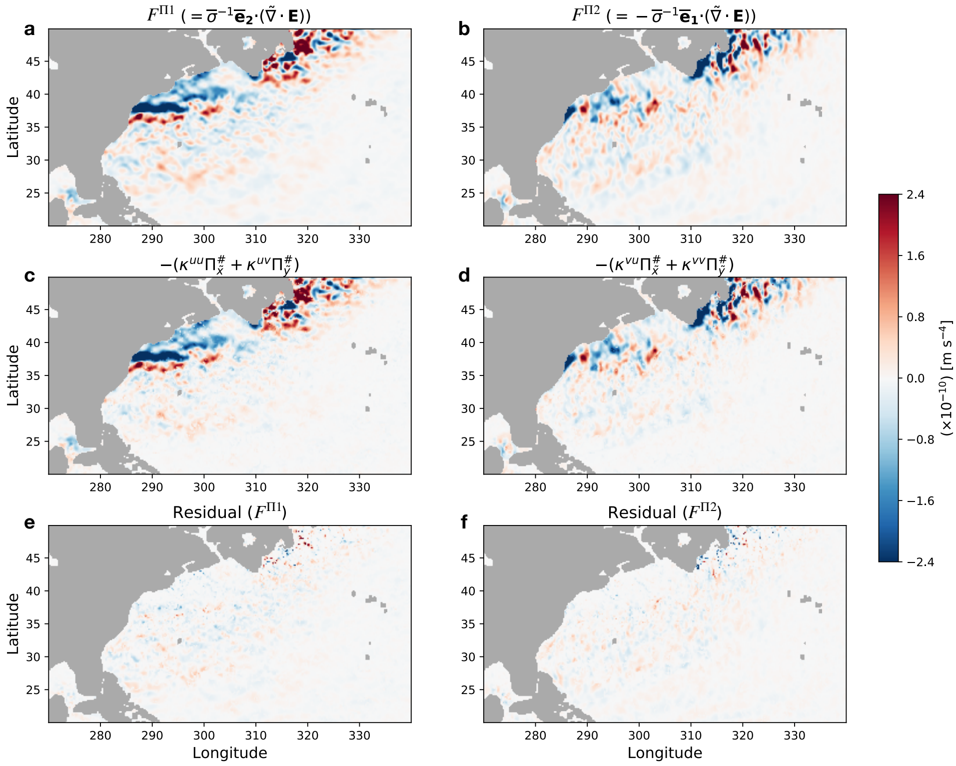

Figure 6. The diagnosed zonal and meridional eddy PV flux on January 3, 2008 on the isosurface of buoyancy as in Figure 2 where $\mathbf{F}^{\Pi}$ $(= \; F^{\Pi 1}\overline{\mathbf{e}}_1 + F^{\Pi 2}\overline{\mathbf{e}}_2)$ is the smoothed $\mathbf{F}^{\#}$. We see a strong signal in the Gulf Stream region **a**,**b**. **c**,**d** The reconstructed eddy PV flux via equation (25). **e**,**f** The residual between the true and reconstructed eddy PV flux.

elling studies (Wilson & Williams, 2006; S. K. Smith & Marshall, 2009; Liu et al., 2012; Abernathey et al., 2013; Bachman & Fox-Kemper, 2013; Bachman et al., 2020; Nummelin et al., 2020), which range spatially between $O(10^2–10^6)$ [m^2 s^{-1}]. The negative values, however, may come as a surprise. One of the key differences from the satellite and in-situ observation based estimates is that we do not assume an isotropic down-gradient flux closure with a scalar diffusivity. In other words, the negative "κ"s do not necessarily translate to up-gradient tracer fluxes as, based on equation (25), the closure is a linear combination of the zonal and meridional gradients; the fluxes could be down gradient in the two-dimensional sense. On the other hand, in cases where the eddy fluxes are locally oriented up gradient of the mean tracer field, negative "κ"s would be a faithful representation of this. We show the inner angle between the smoothed eddy flux and gradient of the mean field:

$$\varphi^C = \arccos\left[\frac{\mathbf{F}^C \cdot \mathbf{G}^C}{|\mathbf{F}^C||\mathbf{G}^C|}\right], \tag{26}$$

in Figure 8 for each tracer; a down-gradient eddy flux would result in $\varphi \sim 0$. There are regions of both down-gradient and up-gradient eddy fluxes on the spatial scales as seen in the diffusivities for all three tracers (Figures 7a-d and 8). Although the eddy fluxes should be down gradient of the mean field in the global sense in order to allow for the homogenization of tracers (D. P. Marshall et al., 2012; J. R. Maddison & Marshall, 2013), a locally up-gradient eddy flux is associated with an up-gradient transfer of tracer variance. It should not be surprising that in a realistic simulation, instantaneous fields of tracer variance can be spatially inhomogenous with sources, sinks and transport of variance (Wilson & Williams, 2006; Chen & Waterman, 2017; Bachman et al., 2020). In the context of energy-backscattering eddy parametrizations, when the tracer is Ertel PV, an up-gradient eddy flux is equivalent to the eddies fluxing momentum back into the mean flow, which is precisely the effect we would want to represent.

It is also informative to examine the diffusive component of the diffusivity tensor in regards to isopycnic tracer mixing, i.e. the eigenvalues of the symmetric part of the tensor ($\mathbf{S} \stackrel{\text{def}}{=} (\mathbf{K}+\mathbf{K}^{\mathrm{T}})/2$ where $\mathbf{K}^{\mathrm{T}}$ is the transpose). Since equation (25) only includes isopycnic eddy fluxes, the eigenvectors of $\mathbf{S}$ indicate in which direction the eddies tend to stir the tracers along buoyancy planes with a diffusivity corresponding to each eigenvalue. The spatial median of the eigenvalues along the major-axis (λ^M) and minor-axis (λ^m) of eigenvectors on January 3, 2008 (Figure 7e,f) are 2363.4 (8370.7) m^2 s^{-1} and 110.0 (1694.6) m^2 s^{-1} respectively with a long tail in both positive and negative values.

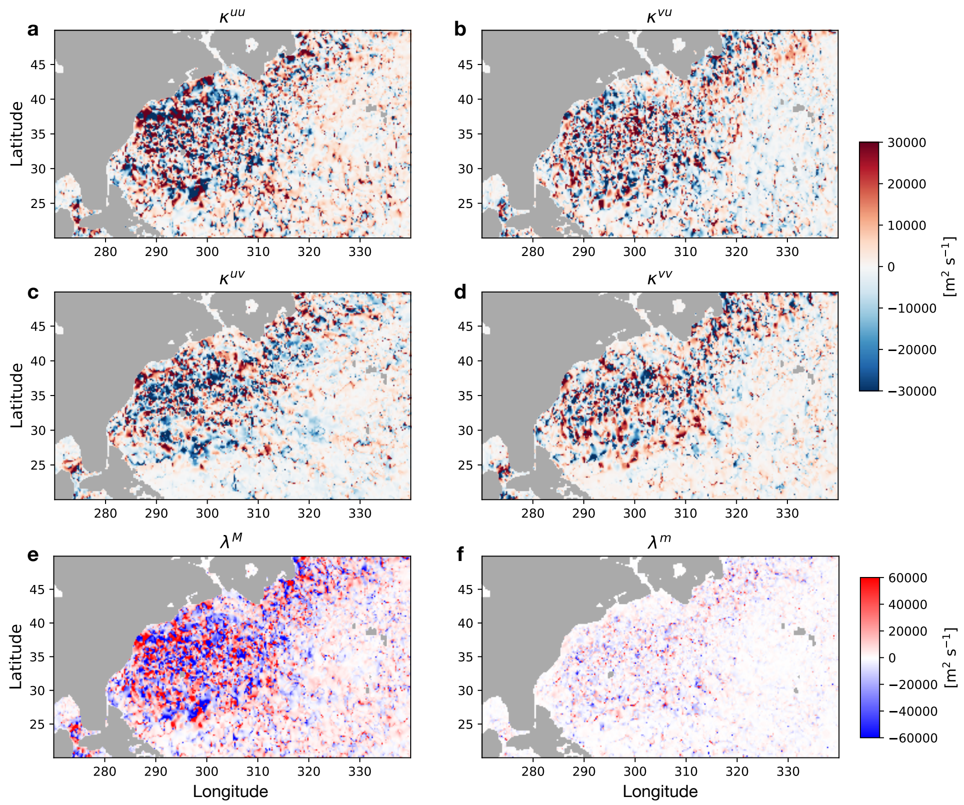

Figure 7. The diagnosed eddy diffusivity parameters via equation (25) in the diffusivity tensor **K** on January 3, 2008 on the iso-surface of buoyancy as in Figure 2 **a**-**d**. **e**,**f** The major- and minor-axis eigenvalues of the diffusivity tensor.

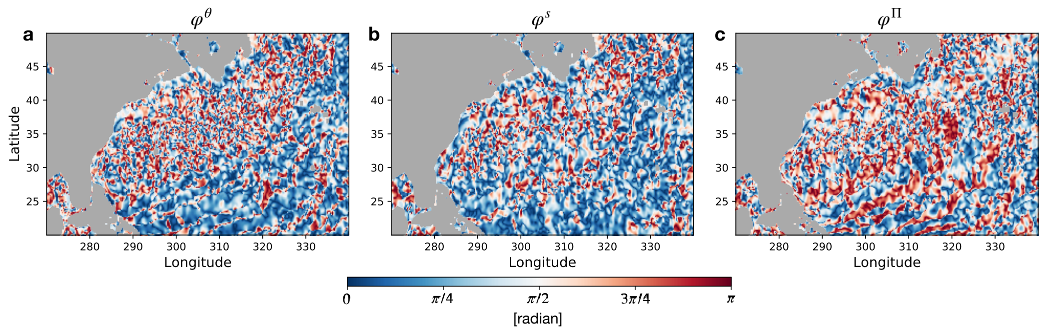

Figure 8. The inner angle between the eddy flux and horizontal gradient of the mean on January 3, 2008 for potential temperature (φ^{θ}) **a**, practical salinity (φ^{s}) **b** and Ertel PV (φ^{Π}) **c** on the buoyancy layer as in Figure 2. The angles are close to zero when the eddy flux is oriented down gradient of the mean Ertel PV and close to π when oriented up gradient.

The values in round brackets show the median of the normed diffusivities $|\lambda^M|$ and $|\lambda^m|$ respectively and do not show a clear seasonality (Figure 9a). The negative values likely come from the mean flow being strongly inhomogeneous. The spatial median of the anisotropy parameter ($|\lambda^M|/|\lambda^m|$) is around 4.37. Although the order of magnitude of the eigenvalues is similar to previous modelling studies (e.g. Abernathey et al., 2013; Bachman et al., 2020), it is difficult to make a direct comparison due to the differences in the averaging operator and model configuration.

We end this section by quantifying the performance of reconstructing the eddy fluxes and show the spatial correlation and error between the true and reconstructed flux along the temporal and buoyancy dimensions:

$$r^C = \frac{\sum\left[(F^C - \langle F^C\rangle)(F^C_{\text{reconstructed}} - \langle F^C_{\text{reconstructed}}\rangle)\right]}{\sqrt{\sum(F^C - \langle F^C\rangle)^2}\sqrt{\sum(F^C_{\text{reconstructed}} - \langle F^C_{\text{reconstructed}}\rangle)^2}}\,, \tag{27}$$

$$\mathcal{E}^C \stackrel{\text{def}}{=} \frac{|F^C - F^C_{\text{reconstructed}}|}{|F^C|}, \tag{28}$$

where $\langle\cdot\rangle$ is the horizontal domain average and the summation ($\sum$) is taken over the horizontal spatial dimension. The spatial correlation and error metric complement one another as r^C is sensitive to extrema due its dependence on the spatial mean and $\mathcal{E}^C$ is sensitive to very small values of eddy fluxes in its dominator (Figure C3). Equations (27) and (28) were calculated using every three grid points in the zonal and meridional dimension between 20°N-50°N and 270°E-340°E, and every two grid points in the buoyancy dimension across the range roughly corresponding to depths between 300–2000 m. The correlation is generally higher than 0.3 for all three tracers across all seasons in the quasi-adiabatic interior for the five years of output we analyze (Figure 9b). The correlation of Ertel PV shows a seasonal cycle where it decreases over the winter (December-April) but is higher than 0.9 for the other seasons which is quite remarkable. During wintertime, the MLD deepens making the fluctuation of thickness (σ) near the surface large; the increase in correlation can be seen with depth (Figure 9d). The large temporal fluctuations in correlation is likely due to extrema values (Figure 9b) as the spatial median of the error is stable over the entire time series (Figure 9c). The robustness of our diagnosed diffusivities can also be seen from the vertical structure of the error (Figure 9e,g,i); it shows very little temporal variation regardless of the date.

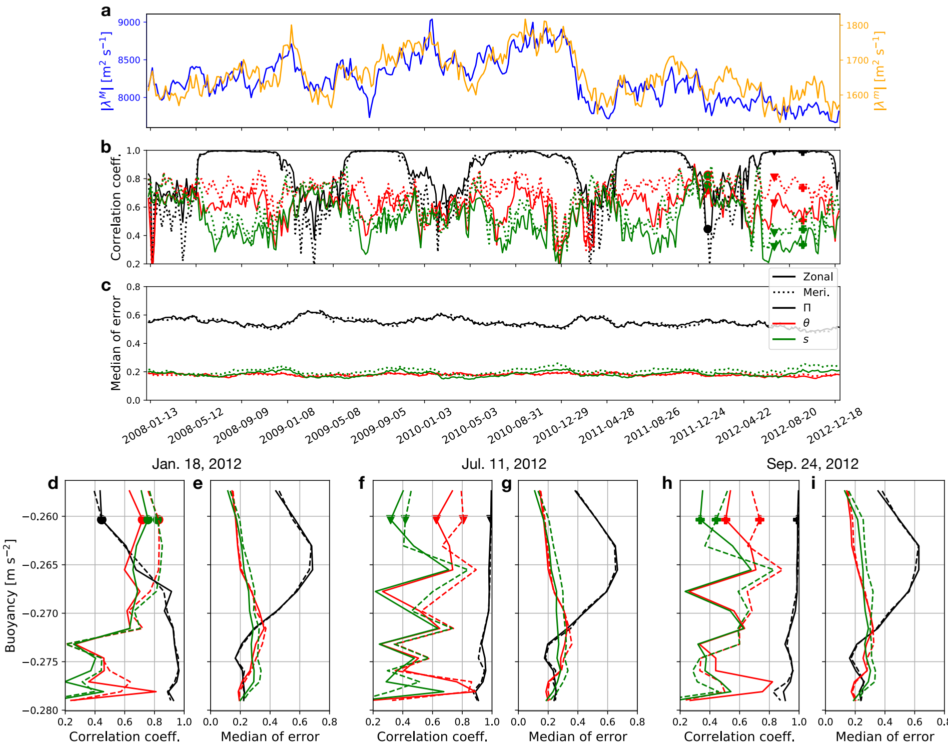

Figure 9. Timeseries of the spatial median of the normed major eigenvalue of the diffusivity tensor on the buoyancy level as in Figure 2 plotted against the left y axis (blue; $|\lambda^M|$) and normed minor eigenvalue plotted against the right y axis (orange; $|\lambda^m|$). Note the difference in the left and right y axes **a**. **b**,**c** The correlation coefficient and spatial median of the error for potential temperature (red; $r^\theta, \mathcal{E}^\theta$), practical salinity (green; $r^s, \mathcal{E}^s$) and Ertel PV (black; $r^\Pi, \mathcal{E}^\Pi$). The zonal component is shown in solid lines and the meridional in dotted lines. The correlation coefficients and error on the buoyancy level as in Figure 2. The circle, triangle and plus markers indicate the dates we show the vertical profiles. **d-i** The vertical profiles on January 18, July 11, and September 24 in 2012.

5 Discussion and summary

By running a 24-member ensemble run of the North Atlantic Ocean at mesoscale-permitting resolution (1/12°), we have shown that the thickness-weighted average (TWA) framework can be employed successfully in diagnosing eddy-mean flow interactions in a realistic ocean simulation. The ensemble approach negates the necessity for any temporal averaging in defining the residual-mean flow; we are able to exclude any temporal variability, such as seasonal and interannual fluctuations, from the eddy term and extract the intrinsic mesoscale variability of the ocean. We show that the Eliassen-Palm (E-P) flux divergence, which encapsulates the eddy feedback onto the mean flow (J. R. Maddison & Marshall, 2013), tends to meridionally accelerate the separated Gulf Stream on its northern flank and decelerate it on its southern flank ($-\overline{\mathbf{e}}_2\cdot(\tilde{\nabla}\cdot\mathbf{E})$; Figures 4h and 5b). Modelling studies with varying spatial resolution have shown that the Gulf Stream tends to overshoot northwards in coarse resolution models (e.g. Lévy et al., 2010; Chassignet & Xu, 2017). This overshooting may partially be attributable to mesoscale eddy feedback, in particular baroclinic instability, which tends to decelerate the separated Gulf Stream on its northern flank ($-E^{21}_{\tilde{b}}$; Figures 4f and 5d), being insufficiently resolved at such resolutions, in addition to submesoscale boundary layer processes (e.g. Renault et al., 2016).

In the TWA framework, the eddy Ertel potential vorticity (PV) flux is directly related to the E-P flux divergence (Young, 2012). In the context of eddy parametrization, this implies that if we can relate the eddy Ertel PV flux to the residual mean fields, one has a solution for the mesoscale eddy closure problem. Zanna et al. (2017) achieve this goal under quasi-geostrophic (QG) and ergodic assumptions where they formulate a closure for the QGPV and invert the streamfunction from it. We show in Figures 6 and 7 that the eddy flux can be locally represented via the residual-mean Ertel PV, a first step towards formulating such closure for primitive equation models. We would like to emphasize that the eddy diffusivities presented in this paper are diagnostic rather than prognostic variables. Future work would need to examine how each parameter in the eddy diffusivity tensor ($\mathbf{K}$; equation (25)) is determined by the residual-mean field for a prognostic eddy closure scheme. Data-driven methods may be a viable way to discover such equations to constrain the "κ"s (e.g. Zhang & Lin, 2018; Zanna & Bolton, 2020). While it is beyond the scope of this study, it would also be interesting to examine the relation between the "κ"s and eddy shape, orientation and/or energy (e.g. D. P. Marshall et al., 2012; Waterman & Lilly, 2015; Chen & Waterman, 2017; Bachman et al., 2017; Anstey & Zanna, 2017; Mak et al., 2018; Poulsen et al., 2019).

Nevertheless, we have shown that the eddy Ertel PV flux can be represented as an active tracer by a local-gradient flux closure across all seasons (Figure 9). The apparent success of our diffusivity tensor lies on the fact that it relates the eddy fluxes to the residual-mean as opposed to the Eulerian-mean fields. As was noted by McDougall and McIntosh (2001) and Young (2012), the TWA framework allows one to shift the focus of eddy parametrization from the buoyancy equation to the momentum equations (1) and (2). What follows is that the tensor $\mathbf{K}$ not only brings together the (eddy-induced) skew-diffusive flux of isopycnal thickness (Gent & Mcwilliams, 1990; Griffies, 1998, hereon referred to as GM) and isopycnic diffusive flux of tracers (Redi, 1982, hereon referred to as Redi), which have conventionally been treated separately, but also includes the eddy momentum fluxes, which energy-backscattering eddy parametrizations are being developed to represent (e.g. Kitsios et al., 2013; Zanna et al., 2017; Berloff, 2018; Bachman et al., 2018; Bachman, 2019; Jansen et al., 2019; Perezhogin, 2019; Zanna & Bolton, 2020; Juricke et al., 2020). There are four parameters in the tensor $\mathbf{K}$, but this is no more than assuming, for example, spatial variability and anisotropy in the GM and Redi diffusivities. Although, the Redi diffusivity has existed longer than GM, there has been much more physical insight into the latter (e.g. Visbeck et al., 1997; Cessi, 2008; Mak et al., 2018); this has left the Redi diffusivity poorly constrained, leading to large uncertainties in the oceanic heat and carbon uptake (Gnanadesikan et al., 2015; Jones & Abernathey, 2019). Being able to treat GM and Redi simultaneously is another strength of our framework in contrast to other closure schemes based on PV (e.g. Eden, 2010; Zanna et al., 2017). We believe our results provide a robust framework to evaluate such newly developed energy-backscattering parametrizations in primitive equation models, i.e. they should be representing the E-P flux divergence, and a first step towards a unified mesoscale eddy closure scheme.

Appendix A Energetics under a non-linear equation of state

The TWA residual-mean horizontal momentum equation in geopotential coordinates neglecting dissipation is (Young, 2012; Ringler et al., 2017):

$$\hat{\mathbf{u}}_t + \mathbf{v}^{\#} \cdot \nabla \hat{\mathbf{u}} + f\mathbf{k} \times \hat{\mathbf{u}} = -\nabla_{\mathrm{h}} \phi^{\#} - \overline{\mathbf{e}} \cdot (\nabla_{\mathrm{h}} \cdot \mathbf{E}), \tag{A1}$$

where $\mathbf{v}^\# \stackrel{\text{def}}{=} \hat{u}\mathbf{i} + \hat{v}\mathbf{j} + w^\#\mathbf{k}$ and $\phi^\# \stackrel{\text{def}}{=} \overline{m}(\tilde{t}, \tilde{x}, \tilde{y}, b^\#(t,x,y,z)) + b^\# z$ are the residual-mean velocity and hydrostatic pressure anomaly. It is important to keep in mind that the "z" here is the ensemble averaged depth of an iso-surface of buoyancy, viz. $z = \overline{\zeta}(\tilde{t}, \tilde{x}, \tilde{y}, b^\#(t,x,y,z))$. The residual-mean kinetic energy ($K^\# = |\hat{\mathbf{u}}|^2/2$) budget becomes:

$$K_t^\# + \mathbf{v}^\# \cdot \nabla K^\# = -\hat{\mathbf{u}} \cdot \nabla_{\mathrm{h}} \phi^\# - \hat{\mathbf{u}} \cdot \left[\overline{\mathbf{e}} \cdot (\nabla_{\mathrm{h}} \cdot \mathbf{E})\right] \tag{A2}$$

$$= -\hat{\mathbf{u}} \cdot \nabla_{\mathrm{h}} \phi^\# - w^\# \phi_z^\# + w^\# b^\# - \hat{\mathbf{u}} \cdot \left[\overline{\mathbf{e}} \cdot (\nabla_{\mathrm{h}} \cdot \mathbf{E})\right] \tag{A3}$$

$$= -\mathbf{v}^\# \cdot \nabla \phi^\# + w^\# b^\# - \hat{\mathbf{u}} \cdot \left[\overline{\mathbf{e}} \cdot (\nabla_{\mathrm{h}} \cdot \mathbf{E})\right]. \tag{A4}$$

We can now define the mean dynamic enthalpy as (McDougall, 2003; Young, 2010):

$$h^\# \stackrel{\text{def}}{=} \int_{\Phi_0}^{\Phi^\#} \frac{b^\#(\overline{\theta}, \overline{s}, \Phi^\#)}{g} d\Phi^{\#\prime} = \int_z^0 b^\# dz', \tag{A5}$$

where $\Phi^\# = \Phi_0 - gz$ is the dynamically non-active part of the hydrostatic pressure to be consistent with the Boussinesq approximation. The material derivative of $h^\#(\overline{\theta}, \overline{s}, \Phi^\#)$ is:

$$\frac{D^\#}{Dt} h^\# = h^\#_{\Phi^\#} \frac{D^\# \Phi^\#}{Dt} + h^\#_{\overline{\theta}} \frac{D^\# \overline{\theta}}{Dt} + h^\#_{\overline{s}} \frac{D^\# \overline{s}}{Dt} \tag{A6}$$

$$= h^\#_{\Phi^\#} \Phi_z^\# \frac{D^\# z}{Dt} + h^\#_{\overline{\theta}} \frac{D^\# \overline{\theta}}{Dt} + h^\#_{\overline{s}} \frac{D^\# \overline{s}}{Dt} \tag{A7}$$

$$= -w^\# b^\# + h^\#_{\overline{\theta}} \frac{D^\# \overline{\theta}}{Dt} + h^\#_{\overline{s}} \frac{D^\# \overline{s}}{Dt}. \tag{A8}$$

Therefore,

$$\frac{D^\#}{Dt}(K^\# + h^\#) = -\nabla \cdot \mathbf{v}^\# \phi^\# + \mathcal{H}^\# - \hat{\mathbf{u}} \cdot \left[\overline{\mathbf{e}} \cdot (\nabla_{\mathrm{h}} \cdot \mathbf{E})\right], \tag{A9}$$

where $\mathcal{H}^\# \stackrel{\text{def}}{=} h^\#_{\overline{\theta}} \frac{D^\# \overline{\theta}}{Dt} + h^\#_{\overline{s}} \frac{D^\# \overline{s}}{Dt}$ and we have invoked $\nabla \cdot \mathbf{v}^\# = 0$.

On the other hand, the total kinetic energy budget remapped onto buoyancy coordinate is:

$$\frac{DK}{Dt} = -\tilde{\nabla} \cdot \mathbf{v}\phi + w\tilde{b}, \tag{A10}$$

where $\mathbf{v} \stackrel{\text{def}}{=} v^1 \mathbf{e}_1 + v^2 \mathbf{e}_2 + v^3 \mathbf{e}_3 = u\mathbf{e}_1 + v\mathbf{e}_2 + \left(\varpi + \frac{\zeta_{\tilde{t}}}{\sigma}\right)\mathbf{e}_3$ and $\tilde{\nabla} \cdot \mathbf{v} = \sigma^{-1}\left[(\sigma v^1)_{\tilde{x}} + (\sigma v^2)_{\tilde{y}} + (\sigma v^3)_{\tilde{b}}\right]$ ($= 0$) is the three-dimensional divergence. Defining the dynamic enthalpy in a similar manner as in equation (A5), namely,

$$h = \int_\zeta^0 \tilde{b}\; d\zeta' = \int_{\tilde{b}}^{b_{\text{surf}}} b'\sigma\; db', \tag{A11}$$

yields:

$$\frac{D}{Dt}(K + h) = -\tilde{\nabla} \cdot \mathbf{v}\phi + \mathcal{H}, \tag{A12}$$

where $\mathcal{H} \overset{\text{def}}{=} h_\theta \frac{D\theta}{Dt} + h_s \frac{Ds}{Dt}$. Ensemble averaging after thickness weighting equation (A12) gives:

$$\overline{\sigma \frac{D}{Dt}(K+h)} = -\overline{\sigma \tilde{\nabla} \cdot \mathbf{v}\phi} + \overline{\sigma \mathcal{H}} \tag{A13}$$

$$= -\overline{\sigma}\widehat{\tilde{\nabla} \cdot \mathbf{v}\phi} + \overline{\sigma}\widehat{\mathcal{H}}, \tag{A14}$$

The total kinetic energy can be expanded as:

$$K = \frac{1}{2}|\hat{\mathbf{u}} + \mathbf{u}''|^2 \tag{A15}$$

$$= \frac{|\hat{\mathbf{u}}|^2}{2} + \frac{|\mathbf{u}''|^2}{2} + \hat{u}u'' + \hat{v}v'' \tag{A16}$$

$$\overset{\text{def}}{=} K^{\#} + \mathscr{K} + \hat{u}u'' + \hat{v}v'', \tag{A17}$$

so plugging in equation (A17), and keeping in mind that $\widehat{\widehat{(\cdot)}} = \widehat{(\cdot)}$ and $\overline{\sigma(\cdot)''} = 0$, each term on the left-hand side (LHS) of equation (A14) can be written as:

$$\overline{\sigma \frac{DK}{Dt}} = \overline{\sigma(K_{\tilde{t}} + uK_{\tilde{x}} + vK_{\tilde{y}} + \varpi K_{\tilde{b}})} \tag{A18}$$

$$= (\overline{\sigma K})_{\tilde{t}} + (\overline{\sigma u K})_{\tilde{x}} + (\overline{\sigma v K})_{\tilde{y}} + (\overline{\sigma \varpi K})_{\tilde{b}} \tag{A19}$$

$$= \overline{\sigma}\Big[\frac{D^{\#}}{Dt}(K^{\#} + \widehat{\mathscr{K}}) + \tilde{\nabla} \cdot (\mathbf{J}^K + \hat{u}\mathbf{J}^u + \hat{v}\mathbf{J}^v)\Big], \tag{A20}$$

where $\mathbf{J}^K \overset{\text{def}}{=} \widehat{u''\mathscr{K}}\mathbf{e}_1 + \widehat{v''\mathscr{K}}\mathbf{e}_2 + \widehat{\varpi''\mathscr{K}}\mathbf{e}_3$, $\mathbf{J}^u \overset{\text{def}}{=} \widehat{u''^2}\mathbf{e}_1 + \widehat{v''u''}\mathbf{e}_2 + \widehat{\varpi''u''}\mathbf{e}_3$, $\mathbf{J}^v \overset{\text{def}}{=} \widehat{u''v''}\mathbf{e}_1 + \widehat{v''^2}\mathbf{e}_2 + \widehat{\varpi''v''}\mathbf{e}_3$ are the eddy fluxes of eddy kinetic energy (EKE), eddy zonal and meridional velocities respectively, and

$$\overline{\sigma \frac{Dh}{Dt}} = \overline{\sigma(h_{\tilde{t}} + uh_{\tilde{x}} + vh_{\tilde{y}} + \varpi h_{\tilde{b}})} \tag{A21}$$

$$= (\overline{\sigma h})_{\tilde{t}} + (\overline{\sigma u h})_{\tilde{x}} + (\overline{\sigma v h})_{\tilde{y}} + (\overline{\sigma \varpi h})_{\tilde{b}} \tag{A22}$$

$$= (\overline{\sigma}\hat{h})_{\tilde{t}} + \big[\overline{\sigma}(\hat{u}\hat{h} + \widehat{u''h''})\big]_{\tilde{x}} + \big[\overline{\sigma}(\hat{v}\hat{h} + \widehat{v''h''})\big]_{\tilde{y}} + \big[\overline{\sigma}(\hat{\varpi}\hat{h} + \widehat{\varpi''h''})\big]_{\tilde{b}} \tag{A23}$$

$$= \overline{\sigma}\Big(\frac{D^{\#}}{Dt}\hat{h} + \tilde{\nabla} \cdot \mathbf{J}^h\Big), \tag{A24}$$

where $\mathbf{J}^h \overset{\text{def}}{=} \widehat{u''h''}\mathbf{e}_1 + \widehat{v''h''}\mathbf{e}_2 + \widehat{\varpi''h''}\mathbf{e}_3$ is the eddy flux of fluctuations in dynamic enthalpy, and we have used the relation $\overline{\sigma\phi\theta} = \overline{\sigma}(\hat{\phi}\hat{\theta} + \widehat{\phi''\theta''})$ (equation (72) in Young, 2012). Hence, combining equations (A20) and (A24), equation (A14) becomes:

$$\frac{D^{\#}}{Dt}(K^{\#} + \widehat{\mathscr{K}} + \hat{h}) = -\tilde{\nabla} \cdot (\mathbf{J}^K + \mathbf{J}^h + \hat{u}\mathbf{J}^u + \hat{v}\mathbf{J}^v) - \widehat{\tilde{\nabla} \cdot \mathbf{v}\phi} + \widehat{\mathcal{H}}. \tag{A25}$$

Subtracting equation (A9) from (A25) yields the eddy energy budget:

$$\frac{D^{\#}}{Dt}(\widehat{\mathscr{K}} + \hat{h} - h^{\#}) = -(\widehat{\tilde{\nabla} \cdot \mathbf{v}\phi} - \nabla \cdot \mathbf{v}^{\#}\phi^{\#}) - \tilde{\nabla} \cdot (\mathbf{J}^K + \mathbf{J}^h + \hat{u}\mathbf{J}^u + \hat{v}\mathbf{J}^v)$$
$$+ \widehat{\mathcal{H}} - \mathcal{H}^{\#} + \hat{\mathbf{u}} \cdot \big[\overline{\mathbf{e}} \cdot (\nabla_{\mathrm{h}} \cdot \mathbf{E})\big]. \tag{A26}$$

Equations (A9) and (A26) are the relations derived by Aoki (2014) but for a non-linear EOS and non-zero dia-surface velocity where the residual-mean flow and eddies exchange energy via the E-P flux divergence. It is perhaps interesting to note that h'' is not the eddy potential energy (EPE; $\mathscr{H} \overset{\text{def}}{=} \hat{h} - h^{\#}$ in equation (A26)) and they are related to one another as $h'' = h - (h^{\#} + \mathscr{H})$.

For a linear EOS, the EPE can be rewritten as:

$$\mathscr{H} = -b^{\#}(\hat{\zeta} - \overline{\zeta}) = -b^{\#}\frac{\overline{\sigma'\zeta'}}{\overline{\sigma}}, \tag{A27}$$

by taking advantage of $\hat{h} = -\tilde{b}\hat{\zeta}$, $h^{\#} = -b^{\#}\overline{\zeta}$ and $\tilde{b} = b^{\#}(t, x, y, \overline{\zeta}(\tilde{t}, \tilde{x}, \tilde{y}, \tilde{b}))$. Equation (A27) provides the physical intuition of EPE being defined as the difference between potential energy at the TWA depth ($\hat{\zeta}$) and ensemble-mean depth ($\overline{\zeta}$). In a similar manner, we can also derive:

$$h'' = -\tilde{b}(\zeta - \hat{\zeta}) = -\tilde{b}\zeta'', \tag{A28}$$

and hence, $\overline{h''} = -\mathscr{H}$. Assuming the background buoyancy frequency can be defined as the inverse of ensemble-mean thickness (viz. $\overline{\sigma}^{-1} \sim N^2$) leads to further manipulation of EPE:

$$\mathscr{H} \sim -b^{\#}N^2\overline{\zeta'_{\tilde{b}}\zeta'} = -b^{\#}N^2\left(\frac{\overline{\zeta'^2}}{2}\right)_{\tilde{b}} \tag{A29}$$

$$= -N^2\left[\left(b^{\#}\frac{\overline{\zeta'^2}}{2}\right)_{\tilde{b}} - \frac{\overline{\zeta'^2}}{2}\right], \tag{A30}$$

where the last term in equation (A30) further reduces to the available potential energy under quasi-geostrophic approximation ($b' \sim N^2\zeta'$).

Appendix B Kinematics of discretization

As in Figure B1, imagine u_1 and u_2 are on the same buoyancy contour. The relation between the two is:

$$u_2 = u_1 + u_x\Delta x + u_\zeta\Delta\zeta. \tag{B1}$$

Now,

$$u_{\tilde{x}} \overset{\text{def}}{=} u_x + \frac{\Delta\zeta}{\Delta x}\sigma^{-1}u_{\tilde{b}} \tag{B2}$$

$$= u_x + \frac{\Delta\zeta}{\Delta x}u_\zeta \tag{B3}$$

$$= \frac{u_2 - u_1}{\Delta x} \qquad (\because \text{ equation (B1)}), \tag{B4}$$

so once all of the variables are remapped onto the buoyancy coordinate from geopotential, the discretized horizontal gradients can be taken along the original Cartesian grid.

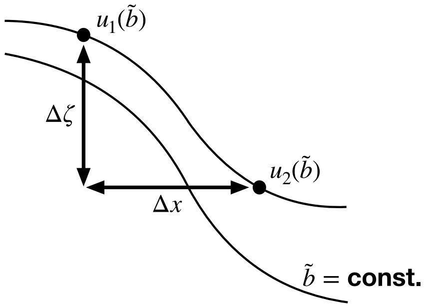

Figure B1. Schematic of discretized gradients.

The gradients on the model outputs were taken using the `xgcm` Python package (Abernathey & Busecke, 2019; Busecke & Abernathey, 2020). In order to minimize the computational cost, we took the ensemble mean first whenever possible, e.g. $\overline{\sigma} = \overline{\partial_{\tilde{b}}\zeta} = \partial_{\tilde{b}}\overline{\zeta}$, $\tilde{\nabla}_{\mathrm{h}}\overline{\sigma} = \partial_{\tilde{b}}\tilde{\nabla}_{\mathrm{h}}\overline{\zeta}$ etc. The gradient operators commuting with the ensemble mean is also the case for the perturbations, i.e.

$$\tilde{\nabla}_{\mathrm{h}}(\overline{m} + m') = \tilde{\nabla}_{\mathrm{h}}m = \overline{\tilde{\nabla}_{\mathrm{h}}m} + (\tilde{\nabla}_{\mathrm{h}}m)'. \tag{B5}$$

Hence, $\tilde{\nabla}_{\mathrm{h}}m' = (\tilde{\nabla}_{\mathrm{h}}m)'$ (cf. J. R. Maddison & Marshall, 2013, Section 2.3 in their paper).

Appendix C Reconstruction of eddy temperature and salinity fluxes

In this section, we show the reconstruction of the eddy temperature and salinity fluxes and the spatial structure of errors for each tracer (equation (28)). Unlike Ertel PV, the strongest signals of eddy temperature and salinity fluxes are in the subpolar gyre (Figures C1 and C2). The spatial structure of the errors also differ amongst the tracers (Figure C3); the errors for Ertel PV are small in the separated Gulf Stream region while as the errors are spread out across the North Atlantic basin for potential temperature and are concentrated within the subtropical gyre for salinity. The banded structure in temperature may be associated with regions of zero-crossing of eddy fluxes. To some extent, the difference in spatial structure implies that the eddy fluxes and local gradient fluxes are not aligned parallel to each other. This provides justification to invert equation (25).

Acknowledgments

This research was funded by the French 'Make Our Planet Great Again' (MOPGA) initiative managed by the Agence Nationale de la Recherche under the Programme d'Investissement

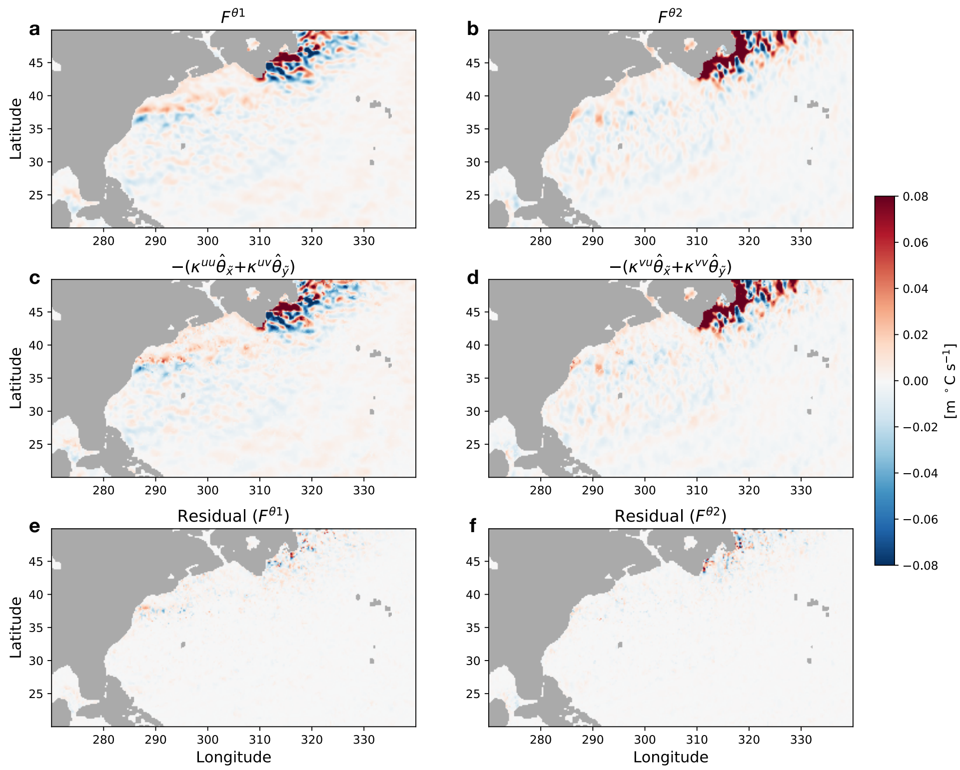

Figure C1. The diagnosed zonal and meridional eddy temperature flux on January 3, 2008 on the iso-surface of buoyancy as in Figure 2 where $\mathbf{F}^{\theta}$ $(= F^{\theta 1}\overline{\mathbf{e}}_1 + F^{\theta 2}\overline{\mathbf{e}}_2)$ is the smoothed $\widehat{\mathbf{u}''\theta''}$ **a**,**b**. **c**,**d** The reconstructed eddy temperature flux via equation (25). **e**,**f** The residual between the true and reconstructed eddy temperature flux.

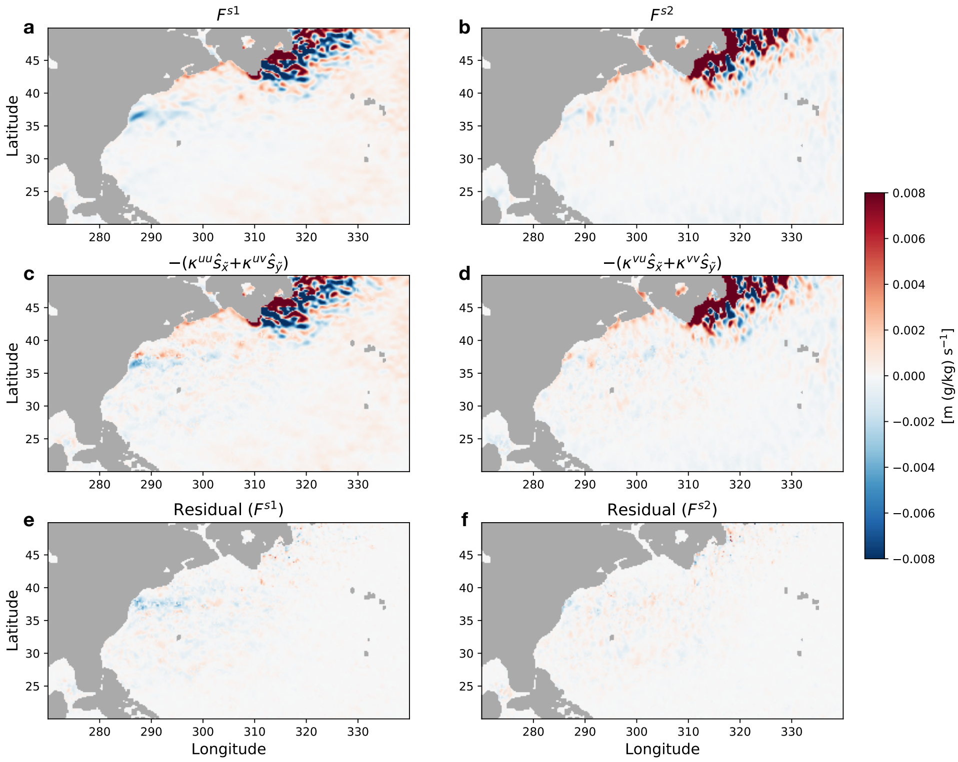

Figure C2. The diagnosed zonal and meridional eddy salinity flux on January 3, 2008 on the iso-surface of buoyancy as in Figure 2 where $\mathbf{F}^s$ $(= \; F^{s1}\overline{\mathbf{e}}_1 \; + \; F^{s2}\overline{\mathbf{e}}_2)$ is the smoothed $\widehat{\mathbf{u}''s''}$ **a**,**b**. **c**,**d** The reconstructed eddy salinity flux via equation (25). **e**,**f** The residual between the true and reconstructed eddy salinity flux.

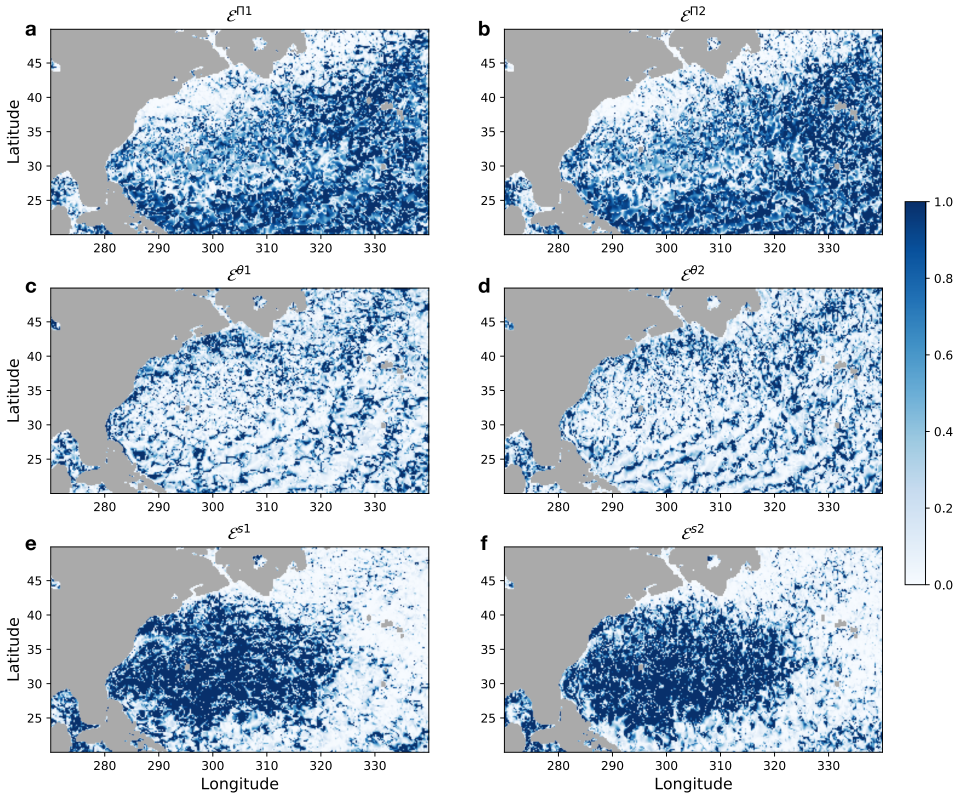

Figure C3. The error due to reconstruction for Ertel PV ($\mathcal{E}^{\Pi}$) **a**,**b**, potential temperature ($\mathcal{E}^{\theta}$) **c**,**d** and practical salinity ($\mathcal{E}^{s}$) **e**,**f** on the iso-surface of buoyancy as in Figure 2 for their zonal and meridional component respectively on January 3, 2008.

d'Avenir, with the reference ANR-18-MPGA-0002. High-performance computing resources on Cheyenne (`doi:10.5065/D6RX99HX`) used for running the ensembles were provided by NCAR's Computational and Information Systems Laboratory, sponsored by the National Science Foundation, under the university large allocation UFSU0011. Dewar acknowledges support from the NSF grants OCE-1829856 and OCE-1941963. Balwada acknowledges support from the NSF grant OCE-1756882. We thank the editor Stephen Griffies, and Laure Zanna along with two other anonymous reviewers for their constructive and careful reviews leading to significant improvements in the manuscript. We would also like to thank Geoffrey Stanley and Trevor McDougall for insightful discussions regarding the buoyancy coordinate for a realistic EOS. The simulation outputs are available on the Florida State University cluster (`http://ocean.fsu.edu/~qjamet/share/data/chaos_amoc_GRL2019/`). Python scripts used for the off-line diagnosis are available on Github (`doi:10.5281/zenodo.4002824`). Uchida acknowledges Spencer Jones for developing the `xlayers` Python package (`doi:10.5281/zenodo.3659227`), Ryan Abernathey and Julius Busecke for the `xgcm` Python package (`doi:10.5281/zenodo.3634752`), and Guillaume Sérazin for the `xscale` Python package for parallelized convolutional spatial filtering (`doi:10.5281/zenodo.322362`).

References

Abernathey, R. P. (2020). `fastjmd95`*: Numba implementation of jackett & mcdougall (1995) ocean equation of state.* Retrieved from `https://github.com/xgcm/fastjmd95`

Abernathey, R. P., & Busecke, J. (2019). `xgcm`*: General circulation model post-processing with xarray.* Retrieved from `https://xgcm.readthedocs.io/en/latest/` doi: 10.5281/zenodo.3634752

Abernathey, R. P., Ferreira, D., & Klocker, A. (2013). Diagnostics of isopycnal mixing in a circumpolar channel. *Ocean Modelling*, *72*, 1–16. doi: 10.1016/j.ocemod.2013.07.004

Abernathey, R. P., & Marshall, J. (2013). Global surface eddy diffusivities derived from satellite altimetry. *Journal of Geophysical Research: Oceans*, *118*(2), 901–916. doi: 10.1002/jgrc.20066

Aiki, H., & Richards, K. J. (2008). Energetics of the global ocean: the role of layer-thickness form drag. *Journal of Physical Oceanography*, *38*(9), 1845–1869. doi: 10.1175/2008JPO3820.1

Ajayi, A., Le Sommer, J., Chassignet, E., Molines, J.-M., Xu, X., Albert, A., & Cosme, E. (2020). Spatial and temporal variability of the north atlantic eddy field from two kilometric-resolution ocean models. *Journal of Geophysical Research: Oceans*. doi: 10.1029/2019JC015827

Aluie, H., Hecht, M., & Vallis, G. K. (2018). Mapping the energy cascade in the north atlantic ocean: The coarse-graining approach. *Journal of Physical Oceanography*, *48*(2), 225–244. doi: 10.1175/JPO-D-17-0100.1

Anstey, J. A., & Zanna, L. (2017). A deformation-based parametrization of ocean mesoscale eddy reynolds stresses. *Ocean Modelling*, *112*, 99–111. doi: 10.1016/j.ocemod.2017.02.004

Aoki, K. (2014). A constraint on the thickness-weighted average equation of motion deduced from energetics. *Journal of Marine Research*, *72*(5), 355–382. doi: 10.1357/002224014815469886

Aoki, K., Kubokawa, A., Furue, R., & Sasaki, H. (2016). Influence of eddy momentum fluxes on the mean flow of the kuroshio extension in a 1/10 ocean general circulation model. *Journal of Physical Oceanography*, *46*(9), 2769–2784. doi: 10.1175/JPO-D-16-0021.1

Arbic, B. K., Polzin, K. L., Scott, R. B., Richman, J. G., & Shriver, J. F. (2013). On eddy viscosity, energy cascades, and the horizontal resolution of gridded satellite altimeter products. *Journal of Physical Oceanography*, *43*(2), 283–300. doi: 10.1175/JPO-D-11-0240.1

Bachman, S. D. (2019). The gm+ e closure: A framework for coupling backscatter with the gent and mcwilliams parameterization. *Ocean Modelling*, *136*, 85–106. doi: 10.1016/j.ocemod.2019.02.006

Bachman, S. D., Anstey, J. A., & Zanna, L. (2018). The relationship between a deformation-based eddy parameterization and the lans-α turbulence model. *Ocean Modelling*, *126*, 56–62. doi: 10.1016/j.ocemod.2018.04.007

Bachman, S. D., & Fox-Kemper, B. (2013). Eddy parameterization challenge suite i: Eady spindown. *Ocean Modelling*, *64*, 12–28. doi: 10.1016/j.ocemod.2012.12.003

Bachman, S. D., Fox-Kemper, B., & Bryan, F. O. (2015). A tracer-based inversion method for diagnosing eddy-induced diffusivity and advection. *Ocean Modelling*, *86*, 1–14. doi: 10.1016/j.ocemod.2014.11.006

Bachman, S. D., Fox-Kemper, B., & Bryan, F. O. (2020). A diagnosis of anisotropic eddy diffusion from a high-resolution global ocean model. *Journal of Advances in Modeling Earth Systems*, *12*(2), e2019MS001904. doi: 10.1029/2019MS001904

Bachman, S. D., Marshall, D. P., Maddison, J. R., & Mak, J. (2017). Evaluation of a scalar eddy transport coefficient based on geometric constraints. *Ocean Modelling*, *109*, 44–54. doi: 10.1016/j.ocemod.2016.12.004

Balwada, D., Smith, S. K., & Abernathey, R. P. (2018). Submesoscale vertical velocities enhance tracer subduction in an idealized antarctic circumpolar current. *Geophysical Research Letters*, *45*(18), 9790–9802. doi: 10.1029/2018GL079244

Berloff, P. (2018). Dynamically consistent parameterization of mesoscale eddies. part iii: Deterministic approach. *Ocean Modelling*, *127*, 1–15. doi: 10.1016/j.ocemod.2018.04.009

Bire, S., & Wolfe, C. L. (2018). The role of eddies in buoyancy-driven eastern boundary currents. *Journal of Physical Oceanography*, *48*(12), 2829–2850. doi: 10.1175/JPO-D-18-0040.1

Bolton, T., Abernathey, R. P., & Zanna, L. (2019). Regional and temporal variability of lateral mixing in the north atlantic. *Journal of Physical Oceanography*, *49*(10), 2601–2614. doi: 10.1175/JPO-D-19-0042.1

Busecke, J., & Abernathey, R. P. (2020). Cmip6 without the interpolation: Grid-native analysis with pangeo in the cloud. In *2020 earthcube annual meeting.* Retrieved from `https://github.com/earthcube2020/ec20_busecke_etal`

Busecke, J., Abernathey, R. P., & Gordon, A. L. (2017). Lateral eddy mixing in the subtropical salinity maxima of the global ocean. *Journal of Physical Oceanography*, *47*(4), 737–754. doi: 10.1175/JPO-D-16-0215.1

Capet, X., McWilliams, J. C., Molemaker, M. J., & Shchepetkin, A. (2008). Mesoscale to submesoscale transition in the california current system. part iii: Energy balance and flux. *Journal of Physical Oceanography*, *38*(10), 2256–2269. doi: https://doi.org/10.1175/2008JPO3810.1

Cessi, P. (2008). An energy-constrained parameterization of eddy buoyancy flux. *Journal of Physical Oceanography*, *38*(8), 1807–1819. doi: 10.1175/2007JPO3812.1

Cessi, P., & Wolfe, C. L. (2013). Adiabatic eastern boundary currents. *Journal of Physical Oceanography*, *43*(6), 1127–1149. doi: 10.1175/JPO-D-12-0211.1

Chassignet, E. P., & Xu, X. (2017). Impact of horizontal resolution (1/12° to 1/50°) on gulf stream separation, penetration, and variability. *Journal of Physical Oceanography*, *47*(8), 1999–2021. doi: 10.1175/JPO-D-17-0031.1

Chen, R., & Waterman, S. (2017). Mixing nonlocality and mixing anisotropy in an idealized western boundary current jet. *Journal of Physical Oceanography*, *47*(12), 3015–3036. doi: 10.1175/JPO-D-17-0011.1

Cole, S. T., Wortham, C., Kunze, E., & Owens, W. B. (2015). Eddy stirring and horizontal diffusivity from argo float observations: Geographic and depth variability. *Geophysical Research Letters*, *42*(10), 3989–3997. doi: 10.1002/2015GL063827

de Boyer Montégut, C., Madec, G., Fischer, A. S., Lazar, A., & Iudicone, D. (2004). Mixed layer depth over the global ocean: An examination of profile data and a profile-based climatology. *Journal of Geophysical Research: Oceans*, *109*(C12). doi: 10.1029/2004JC002378

Deremble, B., Wienders, N., & Dewar, W. (2013). Cheapaml: A simple, atmospheric boundary layer model for use in ocean-only model calculations. *Monthly weather review*, *141*(2), 809–821. doi: 10.1175/MWR-D-11-00254.1

de Szoeke, R. A., & Bennett, A. F. (1993). Microstructure fluxes across density surfaces. *Journal of Physical Oceanography*, *23*(10), 2254–2264. doi: 10.1175/1520-0485(1993)023⟨2254:MFADS⟩2.0.CO;2

de Szoeke, R. A., & Springer, S. R. (2009). The materiality and neutrality of neutral density and orthobaric density. *Journal of Physical Oceanography*, *39*(8), 1779–1799. doi: 10.1175/2009JPO4042.1

Eden, C. (2010). Parameterising meso-scale eddy momentum fluxes based on potential vorticity mixing and a gauge term. *Ocean Modelling*, *32*(1-2), 58–71. doi: 10.1016/j.ocemod.2009.10.008

Eden, C., & Greatbatch, R. J. (2008). Towards a mesoscale eddy closure. *Ocean Modelling*, *20*(3), 223–239. doi: 10.1016/j.ocemod.2007.09.002

Eden, C., Greatbatch, R. J., & Olbers, D. (2007). Interpreting eddy fluxes. *Journal of Physical Oceanography*, *37*(5), 1282–1296. doi: 10.1175/JPO3050.1

Fairall, C. W., Bradley, E. F., Hare, J. E., Grachev, A. A., & Edson, J. B.

(2003). Bulk parameterization of air–sea fluxes: Updates and verification for the coare algorithm. *Journal of climate*, *16*(4), 571–591. doi: 10.1175/1520-0442(2003)016⟨0571:BPOASF⟩2.0.CO;2

Ferrari, R., & Nikurashin, M. (2010). Suppression of eddy diffusivity across jets in the southern ocean. *Journal of Physical Oceanography*, *40*(7), 1501–1519. doi: 10.1175/2010JPO4278.1

Fofonoff, N. (1981). *The gulf stream system. evolution of physical oceanography.* MIT Press. Retrieved from `https://ocw.mit.edu/ans7870/textbooks/Wunsch/Edited/Chapter4.pdf`

Fox-Kemper, B., Lumpkin, R., & Bryan, F. O. (2013). Lateral transport in the ocean interior. In *International geophysics* (Vol. 103, pp. 185–209). Elsevier.

Gent, P. R., & Mcwilliams, J. C. (1990). Isopycnal mixing in ocean circulation models. *Journal of Physical Oceanography*, *20*(1), 150–155. doi: 10.1175/1520-0485(1990)020⟨0150:IMIOCM⟩2.0.CO;2

Gnanadesikan, A., Pradal, M.-A., & Abernathey, R. P. (2015). Isopycnal mixing by mesoscale eddies significantly impacts oceanic anthropogenic carbon uptake. *Geophysical Research Letters*, *42*(11), 4249–4255. doi: 10.1002/2015GL064100

Greatbatch, R. J. (1998). Exploring the relationship between eddy-induced transport velocity, vertical momentum transfer, and the isopycnal flux of potential vorticity. *Journal of Physical Oceanography*, *28*(3), 422–432. doi: 10.1175/1520-0485(1998)028⟨0422:ETRBEI⟩2.0.CO;2

Griffies, S. M. (1998). The gent–mcwilliams skew flux. *Journal of Physical Oceanography*, *28*(5), 831–841. doi: 10.1175/1520-0485(1998)028⟨0831:TGMSF⟩2.0.CO;2

Griffies, S. M. (2004). *Fundamentals of ocean climate models.* Princeton university press.

Griffies, S. M., Winton, M., Anderson, W. G., Benson, R., Delworth, T. L., Dufour, C. O., ... others (2015). Impacts on ocean heat from transient mesoscale eddies in a hierarchy of climate models. *Journal of Climate*, *28*(3), 952–977. doi: 10.1175/JCLI-D-14-00353.1

Groeskamp, S., LaCasce, J. H., McDougall, T. J., & Rogé, M. (2020). Full-depth global estimates of ocean mesoscale eddy mixing from observations and theory. *Geophysical Research Letters*, *47*(18), e2020GL089425. doi: 10.1029/2020GL089425

Grooms, I., & Kleiber, W. (2019). Diagnosing, modeling, and testing a multiplicative stochastic gent-mcwilliams parameterization. *Ocean Modelling*, *133*, 1–10. doi: 10.1016/j.ocemod.2018.10.009

Haynes, P. H., & McIntyre, M. E. (1987). On the evolution of vorticity and potential vorticity in the presence of diabatic heating and frictional or other forces. *Journal of the Atmospheric Sciences*, *44*(5), 828–841. doi: 10.1175/1520-0469(1987)044⟨0828:OTEOVA⟩2.0.CO;2

Jackett, D. R., & Mcdougall, T. J. (1995). Minimal adjustment of hydrographic profiles to achieve static stability. *Journal of Atmospheric and Oceanic Technology*, *12*(2), 381–389. doi: 10.1175/1520-0426(1995)012⟨0381:MAOHPT⟩2.0.CO;2

Jackett, D. R., & McDougall, T. J. (1997). A neutral density variable for the world's oceans. *Journal of Physical Oceanography*, *27*(2), 237–263. doi: 10.1175/1520-0485(1997)027⟨0237:ANDVFT⟩2.0.CO;2

Jamet, Q., Deremble, B., Wienders, N., Uchida, T., & Dewar, W. K. (2021). On wind-driven energetics of subtropical gyres. *Journal of Advances in Modelling Earth Systems*, e2020MS002329. doi: 10.1029/2020MS002329

Jamet, Q., Dewar, W. K., Wienders, N., & Deremble, B. (2019a). Fast warming of the surface ocean under a climatological scenario. *Geophysical Research Letters*, *46*(7), 3871–3879. doi: 10.1029/2019GL082336

Jamet, Q., Dewar, W. K., Wienders, N., & Deremble, B. (2019b). Spatiotemporal patterns of chaos in the atlantic overturning circulation. *Geophysical Research Letters*, *46*(13), 7509–7517. doi: 10.1029/2019GL082552

Jamet, Q., Dewar, W. K., Wienders, N., Deremble, B., Close, S., & Penduff, T. (2020). Locally and remotely forced subtropical amoc variability: A matter of time scales. *Journal of Climate*. doi: 10.1175/JCLI-D-19-0844.1

Jansen, M. F., Adcroft, A., Khani, S., & Kong, H. (2019). Toward an energetically consistent, resolution aware parameterization of ocean mesoscale eddies. *Journal of Advances in Modeling Earth Systems*, *11*(8), 2844–2860. doi: 10.1029/2019MS001750

Jones, S. C. (2019). `xlayers`*: Python implementation of mitgcm's layer package.*

Retrieved from https://github.com/cspencerjones/xlayer doi: 10.5281/zenodo.3659227

Jones, S. C., & Abernathey, R. P. (2019). Isopycnal mixing controls deep ocean ventilation. *Geophysical Research Letters*. doi: 10.1029/2019GL085208

Jones, S. C., Busecke, J., Uchida, T., & Abernathey, R. P. (2020). Vertical regridding and remapping of cmip6 ocean data in the cloud. In *2020 earthcube annual meeting.* Retrieved from https://github.com/earthcube2020/ec20_jones_etal

Juricke, S., Danilov, S., Koldunov, N., Oliver, M., & Sidorenko, D. (2020). Ocean kinetic energy backscatter parametrization on unstructured grids: Impact on global eddy-permitting simulations. *Journal of Advances in Modeling Earth Systems*, *12*(1). doi: 10.1029/2019MS001855

Killworth, P. D. (1997). On the parameterization of eddy transfer part i. theory. *Journal of Marine Research*, *55*(6), 1171–1197. doi: 10.1357/0022240973224102

Kitsios, V., Frederiksen, J. S., & Zidikheri, M. J. (2013). Scaling laws for parameterisations of subgrid eddy–eddy interactions in simulations of oceanic circulations. *Ocean Modelling*, *68*, 88–105. doi: 10.1016/j.ocemod.2013.05.001

Kjellsson, J., & Zanna, L. (2017). The impact of horizontal resolution on energy transfers in global ocean models. *Fluids*, *2*(3), 45. doi: 10.3390/fluids2030045

Klocker, A., & Abernathey, R. P. (2014). Global patterns of mesoscale eddy properties and diffusivities. *Journal of Physical Oceanography*, *44*(3), 1030–1046. doi: 10.1175/JPO-D-13-0159.1

Klocker, A., McDougall, T. J., & Jackett, D. R. (2009). A new method for forming approximately neutral surfaces. , *5*(2), 155–172. doi: 10.5194/os-5-155-2009

Lang, Y., Stanley, G. J., McDougall, T. J., & Barker, P. M. (2020). A pressure-invariant neutral density variable for the world's oceans. *Journal of Physical Oceanography*, 1–58. doi: 10.1175/JPO-D-19-0321.1

Leroux, S., Penduff, T., Bessières, L., Molines, J.-M., Brankart, J.-M., Sérazin, G., … Terray, L. (2018). Intrinsic and atmospherically forced variability of the amoc: insights from a large-ensemble ocean hindcast. *Journal of Climate*, *31*(3), 1183–1203. doi: 10.1175/JCLI-D-17-0168.1

Lévy, M., Klein, P., Tréguier, A.-M., Iovino, D., Madec, G., Masson, S., & Takahashi, K. (2010). Modifications of gyre circulation by sub-mesoscale physics. *Ocean Modelling*, *34*(1-2), 1–15. doi: 10.1016/j.ocemod.2010.04.001

Lévy, M., Resplandy, L., Klein, P., Capet, X., Iovino, D., & Éthé, C. (2012). Grid degradation of submesoscale resolving ocean models: Benefits for offline passive tracer transport. *Ocean Modelling*, *48*, 1–9. doi: 10.1016/j.ocemod.2012.02.004

Liu, C., Köhl, A., & Stammer, D. (2012). Adjoint-based estimation of eddy-induced tracer mixing parameters in the global ocean. *Journal of Physical Oceanography*, *42*(7), 1186–1206. doi: 10.1175/JPO-D-11-0162.1

Maddison, J., Marshall, D., & Shipton, J. (2015). On the dynamical influence of ocean eddy potential vorticity fluxes. *Ocean Modelling*, *92*, 169–182. doi: 10.1016/j.ocemod.2015.06.003

Maddison, J. R., & Marshall, D. P. (2013). The eliassen–palm flux tensor. *Journal of Fluid Mechanics*, *729*, 69–102. doi: 10.1017/jfm.2013.259

Mak, J., Maddison, J. R., & Marshall, D. P. (2016). A new gauge-invariant method for diagnosing eddy diffusivities. *Ocean Modelling*, *104*, 252–268. doi: 10.1016/j.ocemod.2016.06.006

Mak, J., Maddison, J. R., Marshall, D. P., & Munday, D. R. (2018). Implementation of a geometrically informed and energetically constrained mesoscale eddy parameterization in an ocean circulation model. *Journal of Physical Oceanography*, *48*(10), 2363–2382. doi: 10.1175/JPO-D-18-0017.1

Marshall, D. P., Maddison, J. R., & Berloff, P. S. (2012). A framework for parameterizing eddy potential vorticity fluxes. *Journal of Physical Oceanography*, *42*(4), 539–557. doi: 10.1175/JPO-D-11-048.1

Marshall, D. P., Williams, R. G., & Lee, M.-M. (1999). The relation between eddy-induced transport and isopycnic gradients of potential vorticity. *Journal of Physical Oceanography*, *29*(7), 1571–1578. doi: 10.1175/1520-0485(1999)029⟨1571:TRBEIT⟩2.0.CO;2

Marshall, J., Hill, C., Perelman, L., & Adcroft, A. (1997). Hydrostatic, quasi-hydrostatic, and nonhydrostatic ocean modeling. *Journal of Geophysical Research: Oceans*, *102*(C3), 5733-5752. doi: 10.1029/96JC02776

Marshall, J., Shuckburgh, E., Jones, H., & Hill, C. (2006). Estimates and implications of surface eddy diffusivity in the southern ocean derived from tracer transport. *Journal of Physical Oceanography*, *36*(9), 1806–1821. doi: 10.1175/JPO2949.1

McDougall, T. J. (2003). Potential enthalpy: A conservative oceanic variable for evaluating heat content and heat fluxes. *Journal of Physical Oceanography*, *33*(5), 945–963. doi: 10.1175/1520-0485(2003)033⟨0945:PEACOV⟩2.0.CO;2

McDougall, T. J., & Jackett, D. R. (2005). An assessment of orthobaric density in the global ocean. *Journal of Physical Oceanography*, *35*(11), 2054–2075. doi: 10.1175/JPO2796.1

McDougall, T. J., & McIntosh, P. C. (2001). The temporal-residual-mean velocity. part ii: Isopycnal interpretation and the tracer and momentum equations. *Journal of Physical Oceanography*, *31*(5), 1222–1246. doi: 10.1175/1520-0485(2001)031⟨1222:TTRMVP⟩2.0.CO;2

Molines, J.-M., Barnier, B., Penduff, T., Treguier, A., & Le Sommer, J. (2014). Orca12. l46 climatological and interannual simulations forced with dfs4. 4: Gjm02 and mjm88. drakkar group experiment rep. tech. rep. In *Gdri-drakkar-2014-03-19* (p. 50). Retrieved from `http://www.drakkar-ocean.eu/publications/reports/orca12referenceexperiments2014`

Montgomery, R. B. (1937). A suggested method for representing gradient flow in isentropic surfaces. *Bulletin of the American Meteorological Society*, *18*(6-7), 210–212. doi: 10.1175/1520-0477-18.6-7.210

Naveira Garabato, A. C., MacGilchrist, G. A., Brown, P. J., Evans, D. G., Meijers, A. J., & Zika, J. D. (2017). High-latitude ocean ventilation and its role in earth's climate transitions. *Philosophical Transactions of the Royal Society A: Mathematical, Physical and Engineering Sciences*, *375*(2102), 20160324. doi: 10.1098/rsta.2016.0324

Nummelin, A., Busecke, J. J., Haine, T. W., & Abernathey, R. P. (2020). Diagnosing the scale and space dependent horizontal eddy diffusivity at the global surface ocean. *Journal of Physical Oceanography*. doi: 10.1175/JPO-D-19-0256.1

Perezhogin, P. (2019). Deterministic and stochastic parameterizations of kinetic energy backscatter in the nemo ocean model in double-gyre configuration. In *Iop conference series: Earth and environmental science* (Vol. 386, p. 012025). doi: 10.1088/1755-1315/386/1/012025

Plumb, R., & Mahlman, J. (1987). The zonally averaged transport characteristics of the gfdl general circulation/transport model. *Journal of the atmospheric sciences*, *44*(2), 298–327. doi: 10.1175/1520-0469(1987)044⟨0298:TZATCO⟩2.0.CO;2

Poulsen, M. B., Jochum, M., Maddison, J. R., Marshall, D. P., & Nuterman, R. (2019). A geometric interpretation of southern ocean eddy form stress. *Journal of Physical Oceanography*, *49*(10), 2553–2570. doi: 10.1175/JPO-D-18-0220.1

Redi, M. H. (1982). Oceanic isopycnal mixing by coordinate rotation. *Journal of Physical Oceanography*, *12*(10), 1154–1158. doi: 10.1175/1520-0485(1982)012⟨1154:OIMBCR⟩2.0.CO;2

Renault, L., Molemaker, M. J., Gula, J., Masson, S., & McWilliams, J. C. (2016). Control and stabilization of the gulf stream by oceanic current interaction with the atmosphere. *Journal of Physical Oceanography*, *46*(11), 3439–3453. doi: 10.1175/JPO-D-16-0115.1

Ringler, T., Saenz, J. A., Wolfram, P. J., & Van Roekel, L. (2017). A thickness-weighted average perspective of force balance in an idealized circumpolar current. *Journal of Physical Oceanography*, *47*(2), 285–302. doi: 10.1175/JPO-D-16-0096.1

Roach, C. J., Balwada, D., & Speer, K. (2018). Global observations of horizontal mixing from argo float and surface drifter trajectories. *Journal of Geophysical Research: Oceans*, *123*(7), 4560–4575. doi: 10.1029/2018JC013750

Sasaki, H., Klein, P., Qiu, B., & Sasai, Y. (2014). Impact of oceanic-scale interactions on the seasonal modulation of ocean dynamics by the atmosphere. *Nature communications*, *5*(1), 1–8. doi: 10.1038/ncomms6636

Schubert, R., Jonathan, G., Greatbatch, R. J., Baschek, B., & Biastoch, A. (2020). The submesoscale kinetic energy cascade: Mesoscale absorption of submesoscale mixed-layer eddies and frontal downscale fluxes. *Journal of Physical Oceanography*. doi: 10.1175/JPO-D-19-0311.1

Sérazin, G. (2019). `xscale`*: A library of multi-dimensional signal processing tools using parallel computing.* Retrieved from `https://github.com/serazing/xscale` doi: 10.5281/zenodo.322362

Sérazin, G., Jaymond, A., Leroux, S., Penduff, T., Bessières, L., Llovel, W., ... Terray, L. (2017). A global probabilistic study of the ocean heat content low-frequency variability: Atmospheric forcing versus oceanic chaos. *Geophysical*

Research Letters, *44*(11), 5580–5589. doi: 10.1002/2017GL073026

Smith, R. D., & Gent, P. R. (2004). Anisotropic gent–mcwilliams parameterization for ocean models. *Journal of Physical Oceanography*, *34*(11), 2541–2564. doi: 10.1175/JPO2613.1

Smith, S. K., & Marshall, J. (2009). Evidence for enhanced eddy mixing at mid-depth in the southern ocean. *Journal of Physical Oceanography*, *39*(1), 50–69. doi: 10.1175/2008JPO3880.1

Stammer, D. (1997). Global characteristics of ocean variability estimated from regional topex/poseidon altimeter measurements. *Journal of Physical Oceanography*, *27*(8), 1743–1769. doi: 10.1175/1520-0485(1997)027⟨1743:GCOOVE⟩2.0.CO;2

Stanley, G. (2018). *Tales from topological oceans* (Doctoral dissertation, University of Oxford). Retrieved from `https://ora.ox.ac.uk/objects/uuid:414355e6-ba26-4004-bc71-51e4fa5fb1bb`

Stanley, G. J. (2019a). The exact geostrophic streamfunction for neutral surfaces. *Ocean Modelling*, *138*, 107–121. doi: 10.1016/j.ocemod.2019.04.002

Stanley, G. J. (2019b). Neutral surface topology. *Ocean Modelling*, *138*, 88–106. doi: 10.1016/j.ocemod.2019.01.008

Tailleux, R. (2016). Generalized patched potential density and thermodynamic neutral density: Two new physically based quasi-neutral density variables for ocean water masses analyses and circulation studies. *Journal of Physical Oceanography*, *46*(12), 3571–3584. doi: 10.1175/JPO-D-16-0072.1

Uchida, T., Abernathey, R. P., & Smith, S. K. (2017). Seasonality of eddy kinetic energy in an eddy permitting global climate model. *Ocean Modelling*, *118*, 41–58. doi: 10.1016/j.ocemod.2017.08.006

Uchida, T., Balwada, D., Abernathey, R. P., McKinley, G. A., Smith, S. K., & Lévy, M. (2019). The contribution of submesoscale over mesoscale eddy iron transport in the open southern ocean. *Journal of Advances in Modeling Earth Systems*, *11*, 3934–3958. doi: 10.1029/2019MS001805

Uchida, T., Balwada, D., Abernathey, R. P., McKinley, G. A., Smith, S. K., & Lévy, M. (2020). Vertical eddy iron fluxes support primary production in the open southern ocean. *Nature communications*, *11*(1), 1–8. doi: 10.1038/s41467-020-14955-0

Vallis, G. K. (2017). *Atmospheric and oceanic fluid dynamics* (2nd ed.). Cambridge University Press.

Visbeck, M., Marshall, J., Haine, T., & Spall, M. (1997). Specification of eddy transfer coefficients in coarse-resolution ocean circulation models. *Journal of Physical Oceanography*, *27*(3), 381–402. doi: 10.1175/1520-0485(1997)027⟨0381:SOETCI⟩2.0.CO;2

Waterman, S., & Lilly, J. M. (2015). Geometric decomposition of eddy feedbacks in barotropic systems. *Journal of Physical Oceanography*, *45*(4), 1009–1024. doi: 10.1175/JPO-D-14-0177.1

Wilson, C., & Williams, R. G. (2006). When are eddy tracer fluxes directed downgradient? *Journal of Physical Oceanography*, *36*(2), 189–201. doi: 10.1175/JPO2841.1

Xu, Y., & Fu, L.-L. (2011). Global variability of the wavenumber spectrum of oceanic mesoscale turbulence. *Journal of Physical Oceanography*, *41*(4), 802–809. doi: https://doi.org/10.1175/2010JPO4558.1

Xu, Y., & Fu, L.-L. (2012). The effects of altimeter instrument noise on the estimation of the wavenumber spectrum of sea surface height. *Journal of Physical Oceanography*, *42*(12), 2229–2233. doi: 10.1175/JPO-D-12-0106.1

Young, W. R. (2010). Dynamic enthalpy, conservative temperature, and the seawater boussinesq approximation. *Journal of Physical Oceanography*, *40*(2), 394–400. doi: 10.1175/2009JPO4294.1

Young, W. R. (2012). An exact thickness-weighted average formulation of the boussinesq equations. *Journal of Physical Oceanography*, *42*(5), 692–707. doi: 10.1175/JPO-D-11-0102.1

Zanna, L., & Bolton, T. (2020). Data-driven equation discovery of ocean mesoscale closures. *Geophysical Research Letters*, e2020GL088376. doi: 10.1029/2020GL088376

Zanna, L., Mana, P. P., Anstey, J., David, T., & Bolton, T. (2017). Scale-aware deterministic and stochastic parametrizations of eddy-mean flow interaction. *Ocean Modelling*, *111*, 66–80. doi: 10.1016/j.ocemod.2017.01.004

Zhang, S., & Lin, G. (2018). Robust data-driven discovery of governing physical laws with error bars. *Proceedings of the Royal Society A: Mathematical, Physical and Engineering Sciences*, *474*(2217), 20180305. doi: 10.1098/rspa.2018.0305

Zhao, K., & Marshall, D. P. (2020). Ocean eddy energy budget and parameterization in the north atlantic. In *Ocean sciences meeting 2020.* Retrieved from https://agu.confex.com/agu/osm20/meetingapp.cgi/Paper/646129